ABSTRACT

A PRELIMINARY STUDY OF PUMP/PROBE ANGULAR DEPENDENCE OF ZEEMAN ELECTROMAGNETICALLY INDUCED TRANSPARENCY

by Richard Aram Jackson Jr.

This thesis outlines my work to determine the dependence of Zeeman Electromagnetically Induced Transparency (EIT) on the relative angle between the pump and probe beams. We report initial measurements of Zeeman EIT and EIA using a simple arrangement in which the Zeeman sublevels are scanned around fixed pump and probe frequencies. We introduce improvements in magnetic field uniformity and measure EIT/EIA feature lineshape vs. pump/probe angle. Next, we outline our progress on performing Zeeman EIT/EIA experiments in the traditional format, i.e. scanning the probe frequency while holding the pump frequency fixed, which is more amenable to theoretical modeling.

A PRELIMINARY STUDY OF PUMP/PROBE ANGULAR DEPENDENCE OF ZEEMAN ELECTROMAGNETICALLY INDUCED TRANSPARENCY

A Thesis

Submitted to the

faculty of Miami University

In partial fulfillment of

the requirements for the degree of

Master of Science

Department of Physics

by

Richard A. Jackson Jr.

Miami University

Oxford, Ohio

2015

Advisor: _____

(Dr. Samir Bali)

Reader: _____

(Dr. Perry Rice)

Reader: _____

(Dr. James Clemens)

Table of Contents

1. List of Figures

2. Acknowledgements

I wish to thank and acknowledge the following people for their invaluable help:

My undergraduate assistants Kaleb Campbell and Dillon DeMederos for their invaluable partnerships in the lab over these two Summers— This project would not have advanced nearly so much as it has without your dedication. Thank you for your patient learning. I have been privileged to watch you grow over our time together, and can't wait to see the excellent contributions you make as you continue in this and other experiments in the future.

Dr. Samir Bali for being my advisor during my time here— Thank you for your patience with me as I learned the ropes on the ECDL, for aiding me in evaluating my hypotheses, and for your assistance in choosing a direction for this project. Thank you for providing me the opportunity to research such an interesting topic as EIT in your group.

Ethan Clements, Matt Gillette, and Andrew Hachtel— Thank you for teaching me so much in the lab. Thank you for showing me around the tangled mess of homebuilt electronics, for letting me bounce ideas off of you, and for guiding us through installing the AOMs. By your help, you've doubtless saved us weeks of struggling, many trips to the instrumentation lab for repairs, and much guesswork.

Mike Weeks and Jayson Alexander of the Miami University Instrumentation Lab— Thank you for supporting our group with many electronics and physical parts. You've taken on lots of challenging design work for us with a great deal of professionalism, and given us quality and reliable devices for our experiment.

The Lord Jesus Christ, our loving creator— Thank you, Lord, for creating us and giving us such a deep and interesting world to explore; even after many thousands of years we have yet to understand all of its workings and intricacies. Much more importantly, thank you for loving us despite our sin and rebellion against you. Thank you Lord, that although we are sinful even from the time we are conceived, and that although we have failed to keep your just and perfect law, you kept it perfectly for us. Although the wages earned by our sin is death, you took this penalty in our place by your death on the cross. Thank you Lord for being the whole and complete propitiation for our sins, requiring no good work, merit, or worthiness from us. Thank you for saving us by your grace alone, and instilling in us the faith to trust in you alone. (Ephesians 2:1-10)

3. Professional Presentations at Conferences (3 external, 1 internal)

1) Ultrahigh resolution atomic spectroscopy using Electromagnetically Induced Transparency: "Slow light" and ultrasensitive magnetometry: We have experimentally witnessed electromagnetically induced transparency (EIT) in a rubidium vapor cell. The atomic spectral feature natural linewidth of rubidium gas is around 6MHz, but with EIT, we have measured a linewidth as low as 100 kHz. We also minimized the effects of spurious signals in our experiment, which could be falsely identified as an EIT signal. EIT can be used to slow down the speed of light, which is useful in applications such as quantum computing, where EIT could be useful in information storage.

Richard Jackson, Kaleb Campbell, Samir Bali, 2014 Annual Spring Meeting of the APS Ohio-Region Section, Volume 59, Number 3, Friday–Saturday, April 4–5, 2014; Youngstown, Ohio Bulletin of American Physical Society http://meetings.aps.org/link/BAPS.2014.OSS.C1.28

2) Electromagnetically Induced Transparency Experiments for the Advanced Undergraduate Laboratory: Suppression of Polarization Impurity and Stray Magnetic Fields: We investigate electromagnetically induced transparency (EIT) and electromagnetically induced absorption (EIA) in rubidium vapor using a single laser beam and a scanning magnetic field co-aligned with the laser propagation direction. We show that polarization impurity, stray magnetic fields and imperfect optical alignments cause broadening of the EIT/EIA signal and other spurious effects. We describe a systematic approach to minimizing these undesired effects, which produces EIT/EIA signals nearly two orders of magnitude narrower than the natural linewidth.

Richard Jackson, Kaleb Campbell, Matthew VanVleet, Kodi Kuhnash, Bradley Worth, Amanda Day, Samir Bali, Poster, 45th Annual Meeting of the APS Division of Atomic, Molecular and Optical Physics, Vol. 59, #8, Madison, WI, June 2–6, 2014.
R. Jackson and K. Campbell are joint 1st authors.
Bulletin of American Physical Society http://meetings.aps.org/link/BAPS.2014.DAMOP.K1.186

3) Pump/Probe Angular Dependence of Hanle Electromagnetically Induced Transparency: We investigate the dependence of Hanle Electromagnetically Induced Transparency (EIT) on angular separation between pump and probe field propagation directions in room-temperature Rb vapor. We observe the FWHM of probe transmission spectrum and the amplitude of the EIT signal

while varying the angular separation from 0 to 1 milliradian. Following the work of M. Shuker, O. Firstenberg, R. Pugatch, A. Ben-Kish, A. Ron, and N. Davidson, Phys. Rev. A. 76, 023813 (2007), we examine potential applications in information storage and retrieval.

Richard Jackson, Kaleb Campbell, Michael Crescimanno, and Samir Bali, Poster, 46th Annual Meeting of the APS Division of Atomic, Molecular and Optical Physics, Vol. 60, #7, Columbus, OH, June 8–12, 2015.
Bulletin of American Physical Society http://meetings.aps.org/link/BAPS.2014.DAMOP.K1.186

4) Electromagnetically Induced Transparency in Atomic Vapor: Concept and Applications

Electromagnetically Induced Transparency (EIT), first observed in 1991, is a striking quantum phenomenon that arises when two coherent light beams, each tuned to a different atomic transition, are incident on an atom. If the two transitions share the same final state, the probabilities for the atom to absorb either beam interfere. In this case, the probabilities for the two laser beams to be absorbed may perfectly destructively interfere with each other, leaving the atom unable to absorb a photon from either beam. In other words, as a result of the quantum interference, the atom is rendered completely transparent to both laser beams. Note that if one of the laser beams is blocked, the other is perfectly absorbed by the atom, rendering the vapor opaque. In my talk I describe our implementation of EIT, which is aimed toward two applications that are of immense interest. First, for the fledgling technology of quantum information processing, EIT allows the production of "slow light", where the speed of light in the atomic vapor is reduced by more than six orders of magnitude, down to merely a few tens of meters per second. Second, EIT may also have important applications for cardiac arrhythmia diagnosis and prevention, as it can be used in the creation of an ultrasensitive magnetometer capable of detecting magnetic fields at pico-tesla levels such as those produced by a human heart, for example.

Richard Jackson, Oral presentation at Graduate Research Forum, Miami University, November 2014 (Selected as one of the top three oral presentations at the GRF where over 130 graduate students presented their work in oral and poster sessions)

4. Introduction

Recently, much effort within the field of quantum information has been dedicated to quantum computing technology [1,2,3,4,5], particularly with regard to information storage and retrieval. Major goals for these efforts have included developing solid-state qubit storage [6, 7, 8], lengthening effective storage times [9, 10, 11], and reducing information retrieval loss [12, 13, 14]. In order to attain these goals, many experiments are based on the application of a phenomenon called Electromagnetically Induced Transparency (EIT) [12, 15, 16, 17, 18, 19, 20, 21, 22].

In an electromagnetically induced transparent medium, the index of refraction can be on the order of 10^7. This makes EIT an appealing candidate for quantum information manipulation, as it provides a manifold increase in the time available for encoding information onto light [23]. Further, EIT has been used to store a signal beam for later retrieval with good fidelity by enabling or disabling a corresponding control beam, showing promise as an all-optical delay or register for use in an optical computer [24, 25].

The requirement for two separately controllable laser beams exists not just in EIT [26, 27], but in many other areas of research as well, such as optical trapping and cooling [28], optical tweezing [29], measurements of the optical Kerr effect [30], and observation of optical solitons [31]. In practice, those beams always intersect at some finite angle, and beam divergence also contributes to their relative angle. Despite its ubiquitous nature in experiment, effects of two-beam relative angular displacement on spectral linewidth measurement have not been thoroughly studied. In Ref. [32], the authors observe EIT spectral feature linewidths as a function of pump/probe angle where the angle is varied between 0 and 15 milliradians. The authors of Ref. [33] observe EIT linewidths as a function of intensity at a constant pump-probe angle of 6 milliradians.

Furthermore, in the specific context of EIT, Dicke narrowing [34] of spectral features remains relatively unexplored. Dicke narrowing is important in high-precision spectroscopy applications where ultranarrow linewidths are required, such as in atomic clocks [35, 36] and ion trapping [37]. In Ref. [26], the authors observe EIT spectral features at pump/probe angles between 0 and 1 milliradian to study the effect of Dicke narrowing.

This thesis describes experiments to benchmark our experimental apparatus and reports preliminary observations of EIT/EIA lineshapes in an atomic vapor of ^{85}Rb and ^{87}Rb as a function of relative pump/probe angle.

In Chapter 5, we describe methods for observing EIT and EIA in an atomic system and discuss the alkali atoms used in the experiment. In Chapter 6, we explain previous Zeeman EIT experiments within our group, which note the effects of polarization impurity on observed spurious features. In Chapter 7, we observe EIT in the context of large and small relative pump/probe angles, noting the return of Chapter 6's spurious feature at large angles. We then discuss concepts related to relative pump/probe angle and Dicke narrowing. In Chapter 8, we rebuild our experimental apparatus from the ground up after relocating to a new building. Therein, we detail improvements to our experimental apparatus and describe Zeeman EIT/EIA measurements made with circularly polarized pump and probe beams of fixed frequency in a scanning magnetic field configuration. In Chapter 9, we make improvements to magnetic field uniformity and study EIT lineshape as a function of relative angle between pump and probe beams, motivating a change to a traditional configuration wherein the pump frequency is held fixed, and the probe frequency is scanned around resonance. In Chapter 10 and Chapter 11, we discuss progress made towards studying Zeeman EIT in the traditional configuration, and describe a future experiment for studying Dicke Narrowing. Finally, in Chapter 12 we conclude with a summary of our results and future outlook.

5. Background

In this chapter, we introduce background information for EIT and EIA in both the traditional and Zeeman configurations, and describe the ^{85}Rb & ^{87}Rb atomic systems in which our experiment is performed. we also describe previous work in our group, wherein a single linearly polarized beam is used to study Zeeman EIT.

5.1. Electromagnetically Induced Transparency/Absorption

Consider an atom with three states in a Λ-configuration as shown in Figure 5.1 (a). When a photon resonant with the |1> to |2> transition is incident on the atom, it will be absorbed by the atom. Similarly, a photon resonant with the |3> to |2> transition will also be absorbed. Accordingly, a vapor of such atoms is opaque to each of these photons.

Next, consider that both photons are simultaneously incident on the atom. In this case, each photon will try to excite the atom from its respective ground state to a common excited state. Quantum mechanics states that, when there are two different paths to a common final state, the probability amplitudes associated with those paths will interfere. In this case, the probability amplitudes associated with each of the two photons' being absorbed will interfere destructively, preventing either photon from being absorbed. Accordingly, by the inclusion of a second electromagnetic wave, a transparency is induced in a vapor of such atoms. Hence, the phenomenon is named "Electromagnetically Induced Transparency".

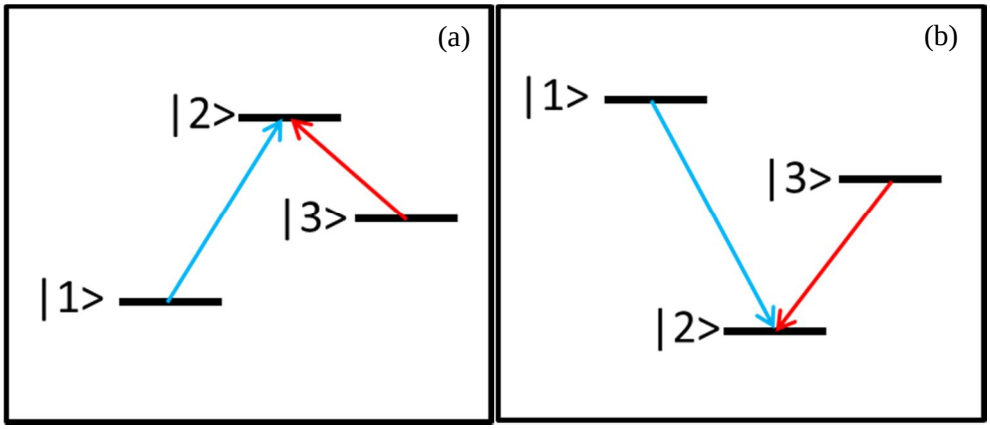

Figure 5.1 Two 3-level atomic system in a (a) Λ- configuration and a (b) V-configuration. Individually, resonant photons will excite transitions between |1> and |2>, and between |3> and |2>, respectively. When co-incident, those same resonant phonons are not absorbed; the probability amplitudes associated with these transitions interfere destructively in (a) EIT or (b) EIA.

Consider now the atom of Figure 5.1 (b), with two excited states and one ground state in a V configuration. Given two incident photons resonant with |1> to |2> and |3> to |2>, respectively, the atom is not induced into a transparent state as in the Λ-configuration case. Rather, the probability amplitudes associated with these transitions destructively interfere, trapping the atom in the excited state and preventing it from undergoing stimulated emission. In this case, only spontaneous emission causes the atom to enter the ground state; only after this spontaneous emission takes place can the atom again absorb a photon. Unlike stimulated emission, however, this spontaneous emission is unlikely to occur in the same direction as the incident photons, effectively causing these photons to be "lost" when observing a transmitted beam's intensity; the induced redirection of stimulated photons to spontaneous emission would appear as a spike in absorption, hence the name "Electromagnetically Induced Absorption".[38]

The above-described schemes for performing EIT and EIA, hereafter referred to as "traditional EIT/EIA", require an amenable atomic level structure that must be addressed by two separate phase-locked laser sources, which greatly complicates the experiment. "Zeeman EIT", described in Chapter 5.2, has been used by many research groups since it (a) creates a convenient structure for EIT & EIA, and (b) can be addressed with different polarizations of a single laser beam, thus greatly simplifying the experiment. Further simplifications, cost- and time-wise, are provided by avoiding the requirement for multiple sets of half and quarter waveplates, separate current and temperature controllers for each laser, synchronization control, etc.

5.2. Zeeman EIT/EIA

It is not necessary to rely on the hyperfine atomic structure to attain EIT and EIA as in the original scheme in Figure 5.1. By applying a magnetic field, the Zeeman effect further splits the hyperfine structure of the atom into many close-lying energy levels as shown in Figure 5.2. Transitions between ground state magnetic sublevels and excited state magnetic sublevels can be addressed using photons of opposite circular polarizations and the same resonant frequency, enabling the use of only one laser and thereby greatly simplifying the experimental apparatus.

We consider the atom of Figure 5.2(b), wherein we denote the m=-1, 0, and +1 ground states to be |a>, |b>, and |c,>, respectively, and denote the excited state to be |d>:

$$|a>=\begin{bmatrix}1\\0\\0\\0\end{bmatrix};|b>=\begin{bmatrix}0\\1\\0\\0\end{bmatrix};|c>=\begin{bmatrix}0\\0\\1\\0\end{bmatrix}and;|d>=\begin{bmatrix}0\\0\\0\\1\end{bmatrix} \quad (1)$$

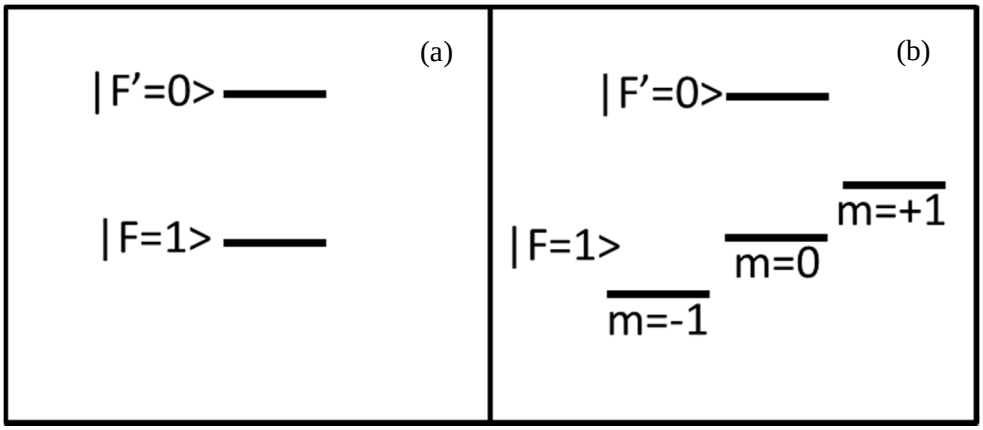

Figure 5.2 Energy level diagram for (a) an undressed two-level system, and (b) the same two-level system, undergoing Zeeman splitting in the presence of a magnetic field; the |F=1> ground state is split into m=-1, 0, and +1 sublevels, while the |F'=0> excited state does not undergo Zeeman splitting.

The Hamiltonian $\mathcal{H}$ for the atom of Figure 5.2(b) is the sum of the bare-atom Hamiltonian $\mathcal{H}_0$, the light-atom interaction $\mathcal{H}_1$, and the magnetic field-atom interaction $\mathcal{H}_B$: $\mathcal{H} = \mathcal{H}_0 + \mathcal{H}_1 + \mathcal{H}_B$ where, for collinear magnetic field and light fields, we obtain

$$\mathcal{H}_0 = \hbar \begin{pmatrix} \omega_g & 0 & 0 & 0 \\ 0 & \omega_g & 0 & 0 \\ 0 & 0 & \omega_g & 0 \\ 0 & 0 & 0 & \omega_e \end{pmatrix} \tag{2}$$

$$\mathcal{H}_1 = \begin{pmatrix} 0 & 0 & 0 & \Omega cos(\omega t) \\ 0 & 0 & 0 & 0 \\ 0 & 0 & 0 & -\Omega cos(\omega t) \\ \Omega cos(\omega t) & 0 & -\Omega cos(\omega t) & 0 \end{pmatrix} \tag{3}$$

$$\mathcal{H}_B = \begin{pmatrix} \Omega_L & 0 & 0 & 0 \\ 0 & 0 & 0 & 0 \\ 0 & 0 & -\Omega_L & 0 \\ 0 & 0 & 0 & 0 \end{pmatrix} \tag{4}$$

ω_g and ω_e are the frequencies associated with the ground and excited states of the bare atom, Ω is the Rabi frequency of the probe transition, ω is the laser frequency, t is time, and Ω_L is the Larmor frequency. Applying the rotating wave approximation and performing the sum, the total Hamiltonian is

$$\mathcal{H} = \hbar \begin{pmatrix} \omega_g + \Omega_L & 0 & 0 & \Omega \\ 0 & \omega_g & 0 & 0 \\ 0 & 0 & \omega_g - \Omega_L & -\Omega \\ \Omega & 0 & -\Omega & \omega_e \end{pmatrix} \tag{5}$$

Let us now consider a population of such atoms

$$\rho = \begin{pmatrix} \rho_{aa} & \rho_{ab} & \rho_{ac} & \rho_{ad} \\ \rho_{ba} & \rho_{bb} & \rho_{bc} & \rho_{bd} \\ \rho_{ca} & \rho_{cb} & \rho_{cc} & \rho_{cd} \\ \rho_{da} & \rho_{db} & \rho_{dc} & \rho_{dd} \end{pmatrix} \tag{6}$$

In order to determine the evolution of the population, we first define the relaxation matrix R to include spontaneous emission Γ from the excited state and decoherence γ due to atoms leaving the laser beam.

$$R = \begin{pmatrix} \gamma & 0 & 0 & 0 \\ 0 & \gamma & 0 & 0 \\ 0 & 0 & \gamma & 0 \\ 0 & 0 & 0 & \gamma + \Gamma \end{pmatrix} \tag{7}$$

We also define the repopulation matrix Λ_Γ to include the same spontaneous decay from the excited state with population ρ_{dd}, and define the repopulation matrix Λ_γ to include atoms entering the laser beam.

$$\Lambda_\Gamma = \begin{pmatrix} \gamma/3 & 0 & 0 & 0 \\ 0 & \gamma/3 & 0 & 0 \\ 0 & 0 & \gamma/3 & 0 \\ 0 & 0 & 0 & 0 \end{pmatrix}, \text{ and } \Lambda_\gamma = \begin{pmatrix} \Gamma\rho_{dd}/3 & 0 & 0 & 0 \\ 0 & \Gamma\rho_{dd}/3 & 0 & 0 \\ 0 & 0 & \Gamma\rho_{dd}/3 & 0 \\ 0 & 0 & 0 & 0 \end{pmatrix} \tag{8}$$

The population density matrix elements then evolve according to

$$\frac{d\rho}{dt} = \frac{1}{i\hbar}[\mathcal{H}, \rho] - \frac{1}{2}\{R, \rho\} + \Lambda_\Gamma + \Lambda_\gamma \tag{9}$$

From the 16 solutions, the population of the excited state evolves according to

$$\dot{\rho}_{dd} = -\frac{1}{2}i\Omega(\rho_{ad} + \rho_{cd} + \rho_{da} - \rho_{dc}) - (\gamma + \Gamma)\rho_{dd} \tag{10}$$

and a few other evolution equations of interest are

$$\begin{aligned} \dot{\rho}_{bb} &= \frac{\gamma}{3} - \gamma\rho_{bb} + \frac{1}{3}\Gamma\rho_{dd} \\ \dot{\rho}_{ad} &= \frac{1}{2}[\gamma\rho_{ad} - (\gamma + \Gamma)\rho_{ad}] - i\Omega_L\rho_{ad} - \frac{1}{2}i\Omega(\rho_{aa} - \rho_{ac} - \rho_{dd}) \\ \dot{\rho}_{cd} &= \frac{1}{2}[\gamma\rho_{cd} - (\gamma + \Gamma)\rho_{cd}] - i\Omega_L\rho_{cd} - \frac{1}{2}i\Omega(\rho_{ca} - \rho_{cc} + \rho_{dd}) \\ \dot{\rho}_{ac} &= -\gamma\rho_{ac} - i\left[2\Omega_L\rho_{ac} - \frac{1}{2}\Omega(\rho_{ad} - \rho_{dc})\right] \end{aligned} \tag{11}$$

From these solutions, we can model the population of the excited state using the Atomic Density Matrix package for Mathematica. Here, we set $\gamma = \frac{v}{r} = 0.015$, using the average thermal velocity of room temperature Rb atoms $v = 240$m/s, and the beam radius $r = 0.43$ mm

measured in Chapter 8.2. We set the pump Rabi frequency to $\chi = 12.68\text{MHz} = 2.09\Gamma$, and the probe Rabi frequency to $\chi = 0.83\text{MHz} = 0.136\Gamma$ to match the pump and probe powers used in Chapter 7 and mimic the powers used in Ref. [39]. We then generate a plot of probe absorption vs. detuning, as shown in Figure 5.3. We measured the FWHM of the EIT feature in the plot to be 0.56Γ.

This plot requires the assumption that only the probe detuning is being scanned, as is the case in the DC magnetic field configuration of Zeeman EIT/EIA, discussed in Chapter 5.2.1 below. However, in the experiments discussed in Chapters 6-9, this is not the case: the experiments of these chapters utilize the scanning magnetic field configuration of Zeeman EIT/EIA discussed in Chapter 5.2.2 below, which effectively scans both the pump and probe detuning concurrently.

In the following sections, we discuss the DC and scanning magnetic field configurations of Zeeman EIT/EIA, and the advantages and disadvantages of each.

5.2.1. DC Magnetic Field

One simple method of attaining Zeeman EIT/EIA is to apply a DC magnetic field to the sample. This causes a static Zeeman splitting of the hyperfine structure.

Experiments using this configuration tune the pump beam to resonance with a desired hyperfine transition, and scan the probe beam frequency around the pump frequency. This method generates EIT/EIA spectra displayed as probe transmission vs probe detuning. Theoretical treatments usually assume the conditions described in this section; see, for example, [32, 33, 39] and the above treatment in Chapter 5.2.

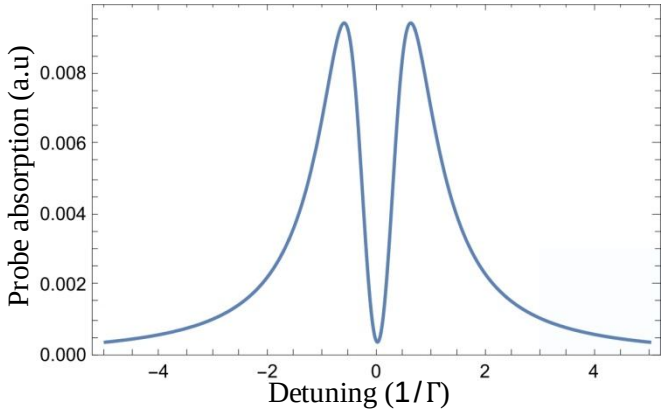

Figure 5.3 Probe absorption vs. probe detuning for pump and probe Rabi frequencies 2.09Γ and 0.136Γ, respectively. The FWHM of the feature is 0.56Γ, or 3.40 MHz for ^{85}Rb and ^{87}Rb.

5.2.2. Scanning Magnetic Field

An alternate method of attaining Zeeman EIT/EIA is to first tune both the pump and probe beams to resonance with the desired transition, and then apply a scanning magnetic field to the sample.

Originally, our group intended to use this scanning magnetic field method as a further simplification to the EIT/EIA scheme; in addition to requiring only one laser source, a scanning magnetic field and fixed pump/probe frequencies removed the need for separate frequency-controlling optics (acousto-optic modulators, associated focusing lenses, precise voltage supply circuitry, etc.) in each of the pump and probe paths.

However, while the experimental apparatus may become extremely simple as a result of scanning the magnetic field, it becomes harder to obtain a simple theoretical understanding of the resulting EIT/EIA lineshapes. The changing Zeeman splitting introduces an effective detuning to both the pump and the probe beams, as shown in Figure 5.4. Although both beams may be in resonance at precisely zero magnetic field, in the presence of a positive/negative magnetic field one of the σ^+/ σ^- now fails to excite a transition, as expected. However, since only probe transmission is typically observed, an asymmetry is introduced in the recorded EIT spectra which is not straightforward to model theoretically. Few theoretical treatments exist that describe the particular situation described in this section (see, for example, Refs. [38, 40, 41, 42, 44]).

In the next section, we consider the hyperfine structure of ^{85}Rb & ^{87}Rb.

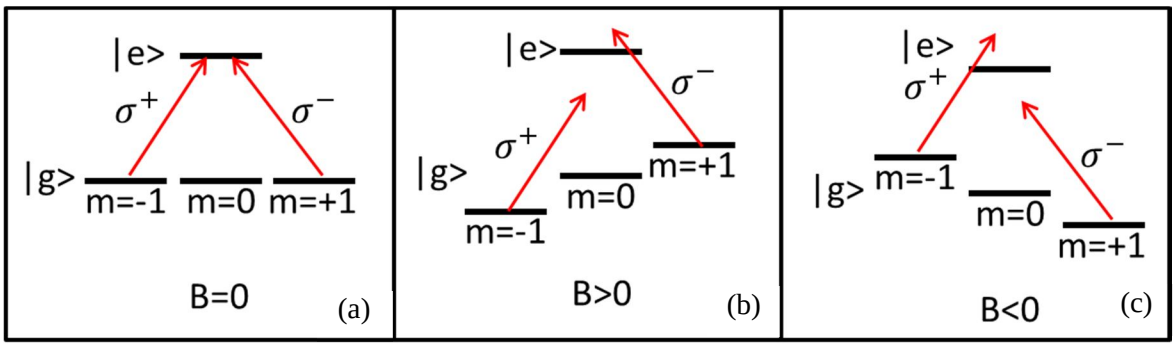

Figure 5.4 Energy level schematic for a two-level system with Zeeman-split ground state. (a) Circularly polarized pump and probe beams tuned to resonance with the system at B=0 generate an EIT feature. (b, c) A positive/negative magnetic field introduces an effective detuning to the pump and probe beams, such that only one of the two photons is likely to excite a transition.

5.3. Atomic System: ^{85}Rb and ^{87}Rb

Throughout this work, room temperature Rb gas of natural isotopic abundance is used to study EIT/EIA. The hyperfine structure ^{85}Rb & ^{87}Rb is shown in Figure 5.5. In particular, we utilize the D2 line ^{85}Rb $F_g=2\rightarrow F_e=1, 2, 3$ and ^{87}Rb $F_g=1\rightarrow F_e=0, 1, 2$ transitions to study EIT, and we use the ^{85}Rb $F_g=3\rightarrow F_e=2, 3, 4$ and ^{87}Rb $F_g=2\rightarrow F_e=1, 2, 3$ transitions to study EIA.

Ideally, experiments involving these transitions would include a laser tuned to resonance with only one excited state, e.g., ^{85}Rb $F_g=2\rightarrow F_e=1$, but not $F_e=2$ or 3. However, spectral features for room temperature Rb atoms are Doppler broadened by about 500MHz. Since the hyperfine separations on Rb's D2 lines are less than this (see Figure 5.5), several transitions are excited off-resonantly by a photon resonant with the target transition.

In order to determine whether a given set of transitions will yield an EIT feature or an EIA feature, it is necessary to consider each transition individually, determine whether the transition would yield EIT or EIA in isolation, and then determine the contribution of that transition to the overall spectral feature. Below, we follow the method outlined in Ref. [38].

When a hyperfine energy level of a given F number undergoes Zeeman splitting, the number of resultant magnetic sublevels is 2F+1. Whether a given transition will yield a Zeeman

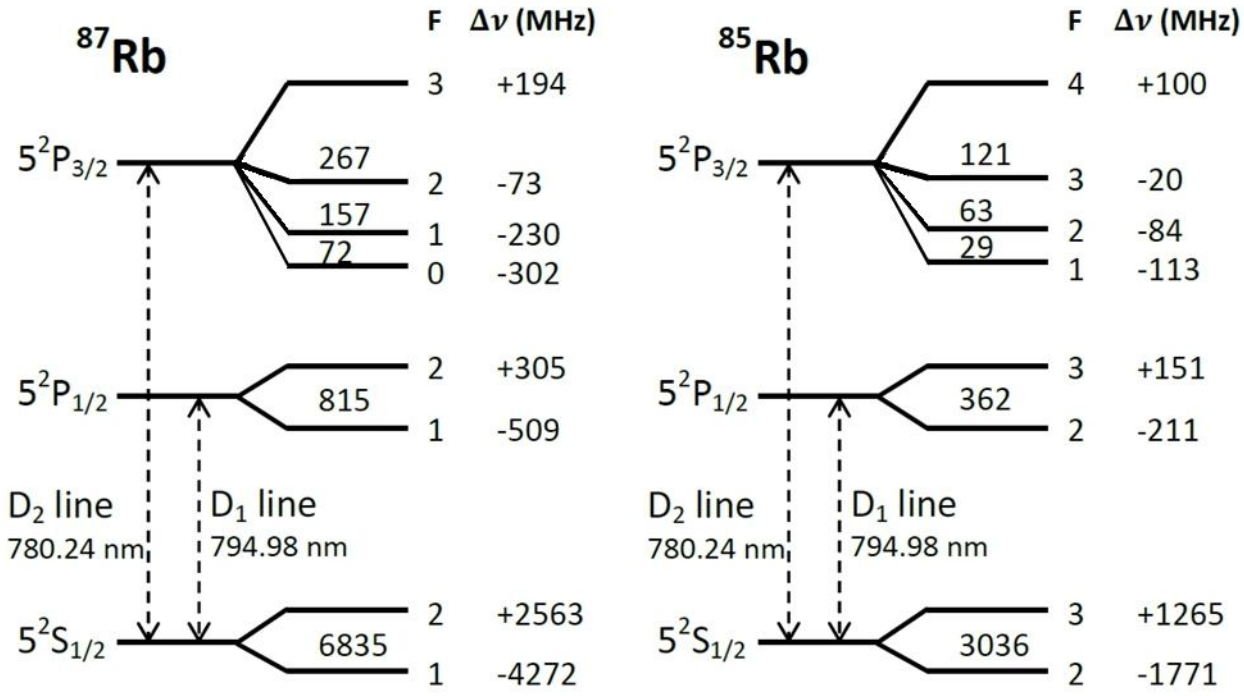

Figure 5.5 Hyperfine structure of ^{85}Rb and ^{87}Rb. In the experiments discussed in this thesis, we exclusively use the D2 line transitions. Figure reproduced from [44].

EIT or EIA feature can be determined by looking at the number of magnetic sublevels of the ground state and comparing to the number of magnetic sublevels in the excited state. If there are more magnetic sublevels in the upper state (F_e) than in the lower (F_g), optical pumping by a strong pump beam will force the atom into three states in a V-like configuration, yielding EIA. If there are more magnetic sublevels in the lower state, then optical pumping forces the atom instead into a Λ-like configuration. If the number of upper and lower magnetic sublevels are equal (i.e., $F_e = F_g$) , then we obtain a net EIT effect. This is because EIT and EIA are both instigated in the $F_e = F_g$ case, but EIT is the more robust of the two, since the atom evolves toward a superposition of ground states and stays there. In EIA on the other hand, the atom evolves toward a superposition of excited states, which must decay eventually owing to spontaneous emission. For example, for the D2 line of ^{85}Rb, the $F_g=3 \rightarrow F_e=2, 3, 4$ transitions yield EIT, EIT, and EIA, respectively.

The relative strengths of EIT/EIA transitions, seen in Figure 5.6, then determine the overall effect. For example, in the specific group of ^{85}Rb transitions $F_g=3 \rightarrow F_e=2, 3, 4$, the combined strength of the $F_g=3 \rightarrow F_e=2$ and $F_g=3 \rightarrow F_e=3$ EIT features does not exceed the strength

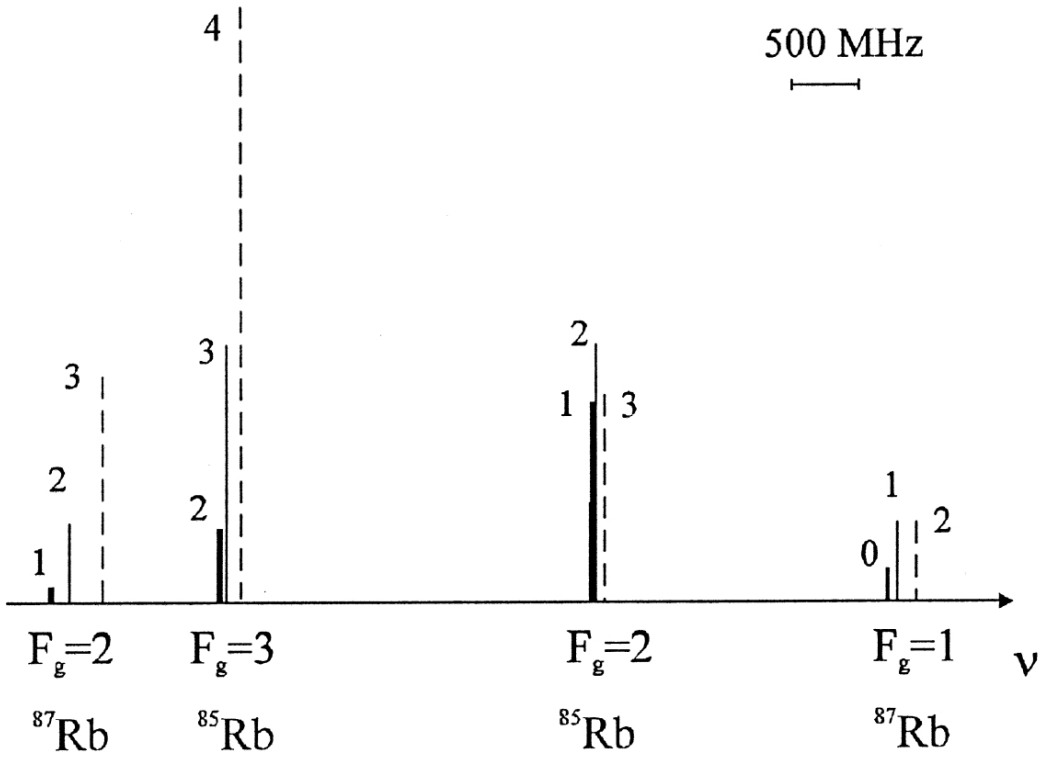

Figure 5.6 Relative strengths for D2 transitions in ^{85}Rb and ^{87}Rb. Reproduced from [38].

of the $F_g=3 \rightarrow F_e=4$ EIA feature. Thus, this particular group of transitions yields a net EIA spectral feature. The same situation is encountered with the $F_g=2 \rightarrow F_e=1, 2, 3$ group of transitions in ^{87}Rb, where again we predict a net EIA feature. On the other hand, we notice that net EIT is predicted for the ^{85}Rb $F_g=2 \rightarrow F_e=1, 2, 3$ and ^{87}Rb $F_g=1 \rightarrow F_e=0, 1, 2$ transitions.

In the next section, we consider the Zeeman splitting associated with these transitions.

5.4. Consideration of Zeeman Shift

In order to determine an effective pump or probe detuning in MHz, the Zeeman splitting associated with the hyperfine transition of interest must be determined. The splitting associated with a given hyperfine transition depends on the Zeeman splitting of both the ground state and excited state energy levels. Each hyperfine energy level has an associated Zeeman splitting factor, which we obtain from Refs. [48,49].

Consider the ^{85}Rb $F_g=2 \rightarrow F_e=2$ transition, shown in Figure 5.7. The Zeeman splitting factor associated with the $F_g=2$ ground state is -0.47 MHz/G, and that of the $F_e=2$ excited state is 0.16 MHz/G. If a magnetic field of 1 Gauss is applied to the atom, the $|F_g=2\ m=+2\rangle$ ground state will shift downward by 2 * 0.47 MHz, and the $|F_e=2, m=+2\rangle$ ground state will shift upward by 2 * 0.16 MHz/G, for a total splitting between these levels of 1.26 MHz; the total Zeeman factor associated with this transition is then 1.26 MHz/G. However, under the influence of the magnetic field, the atoms observe instead the σ^+- and σ^--excited transitions $|F_g=2\ m=+1\rangle \rightarrow |F_e=2, m=+2\rangle$ and $|F_g=2, m=+2\rangle \rightarrow |F_e=2, m=+1\rangle$, respectively. For the former transition, the Zeeman sublevels shift down by (1)(0.47 MHz) (for $|F_g=2\ m=+1\rangle$) and up by (2)(0.16 MHz) (for $|F_e=2, m=+2\rangle$), for a total Zeeman splitting of 0.79MHz/G. For the latter the Zeeman sublevels shift

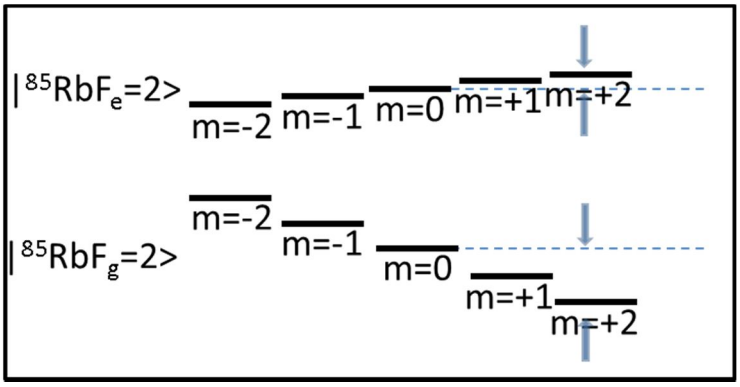

Figure 5.7 Energy level diagram for ^{85}Rb D2-line $F_g=2$ and $F_e=2$, showing Zeeman sublevels. As the ground and excited states have different associated Zeeman splittings, the rightmost Zeeman sublevels are shifted by different amounts.

down by (2)(0.47 MHz) (for $|F_g=2, m=+2\rangle$) and up by (1)(0.16 MHz) ($|F_e=2, m=+1\rangle$), for a total Zeeman splitting of 1.10MHz/G.

For the groups of transitions used in this study, ^{85}Rb $F_g=2 \rightarrow F_e=1, 2, 3$ and ^{85}Rb $F_g=3 \rightarrow F_e=2, 3, 4$, as well as ^{87}Rb $F_g=1 \rightarrow F_e=0, 1, 2$ and ^{87}Rb $F_g=2 \rightarrow F_e=1, 2, 3$, each of the transitions involved will experience different Zeeman splitting under the same magnetic field. This complicates efforts to assign an appropriate Zeeman shift to each of the four transition groups. To do this, we select one dominant transition within each group, and then calculate the Zeeman splitting associated with that transition. For example, the dominant transition in the ^{85}Rb $F_g=2 \rightarrow F_e=1, 2, 3$ group (from Figure 5.6) is the ^{85}Rb $F_g=2 \rightarrow F_e=2$ transition, so we can determine the Zeeman splitting as shown in the previous paragraph.

In the case of a strong σ^+ pump and weak σ^- probe, the ^{85}Rb EIT effect will come from the rightmost levels $|F_g=2\ m=+2\rangle$, $|F_g=2\ m=0\rangle$, and $|F_e=2\ m=+1\rangle$, with associated ground-state Zeeman shifts of 1.10 MHz/G and 0.16 MHz/G. Unfortunately, this results in *both the pump and probe detuning changing at different rates* in the scanning magnetic field configuration. This greatly complicates understanding of the feature width in this configuration.

In previous works by our group, the authors of Refs. [48], [49], and [50] calculated linewidths of EIT and EIA features using only the Zeeman shift of the ground state, and then assuming the m=+1 magnetic sublevel (e.g., $(+1)(0.47\ MHz/Gauss) = 0.47\ MHz/Gauss$ for ^{85}Rb $F_g=2 \rightarrow F_e=1, 2, 3$). In this manner, they erroneously claimed subnatural EIT/EIA linewidths on the order of 100-300kHz. In order to accurately describe observed feature lineshapes in Chapters 8 and 9, we report our measurements of EIT/EIA feature widths obtained using the scanning magnetic field configuration in terms of the magnetic field strength.

This consideration further motivates the study of Zeeman EIT/EIA in the DC magnetic field configuration, wherein the pump can be held fixed in resonance with one transition, and the probe detuning can be scanned independently. We begin modifying the apparatus to use the DC magnetic field configuration in Chapter 10. In the next section, we discuss the construction of our laser source, and how frequency tuning of the pump and probe beams is achieved experimentally.

5.5. Frequency-tunable Laser Source

The laser source used in our experiment is a homebuilt external cavity diode laser (ECDL) modeled after the laser system discussed in Ref. [47], pictured in Figure 5.8. In this system, a laser diode is mounted on a movable arm, whose movement adjusts a distance between the laser diode and a collimating lens. Collimated light from the diode travels through a 50/50 beamsplitter to a diffraction grating, which feeds back light into the laser diode. By adjusting the angle of the diffraction grating, the frequency of the light fed back into the diode can be adjusted, so as to seed the diode output with light of the desired frequency.

Half of the light output by the diode reflects off of the 50/50 beamsplitter interface, and out through a window in the housing, defining the primary output of the system to be used for the experiment. Half of the light from the diffraction grating strikes the 50/50 beamsplitter interface, and is directed by a mirror out through a separate window in the housing, defining a secondary output to be used for saturated absorption spectroscopy (SAS).

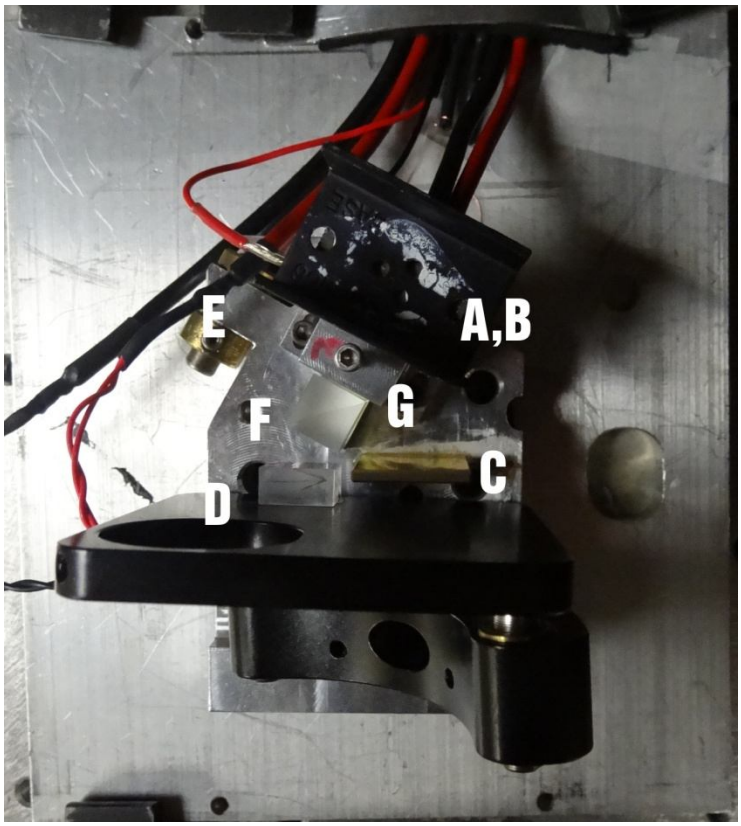

Figure 5.8 The ECDL used in our experiment. (A) A thermal heat sink, mounted on top of (B) a mounted laser diode. (C) A mirror for directing light through a secondary output window in the housing. (D) A Blazed diffraction grating for feeding back light into the laser diode. (E) A collimation screw for finely adjusting the distance between the laser diode and the collimating lens.

(F) A 50/50 beamsplitter for directing light to a primary output window in the housing. (G) A lens for collimating the laser diode output.

In Ref. [47], a blazed diffraction grating is used for the purpose of preferentially putting more power into an output direction (the zero-order reflection), and less power into the feedback direction. The author of Ref. [47] refers to this as the "low feedback-large output configuration". However, the zero-order reflection is not used in our system, so it is disadvantageous to direct more power in that reflection.

To correct this, we have flipped the diffraction grating such that it directs more power into the m=-1 order. Since this order is used for feedback into the diode, this change was thought to improve the tuning range of the system; this is particularly important in trying to tune our 785nm laser diodes to resonance with the Rb D2 line (780.1nm). Additionally, the increase in feedback should provide additional seed power, boosting the output light that will be reflected off of the 50/50 beamsplitter.

In the next section, we briefly discuss observations of Zeeman EIT with a single linearly polarized laser beam made by previous researchers in our group, who noted a requirement for a high degree of polarization purity.

6. Previous Observations with a Single Linearly Polarized Beam

Our research group previously studied Zeeman EIT/EIA on the D2 line of ^{85}Rb and ^{87}Rb using a single linearly polarized beam via the scanning magnetic field method described in Chapter 5.2.2. This linearly polarized beam is observed by the atoms as a superposition of left and right circularly polarized beams, one of which is designated as the 'pump' component and the other as the 'probe' component. In Refs. [49] and [50], both researchers noted a spurious EIT-like signal – spurious because this signal was observed when the input beam was purely circularly polarized, either fully σ^+ or σ^- – and reasoned that this spurious signal arises from (a) polarization impurity of optical elements, and (b) misalignment of the input beam with the co-linear magnetic field applied to the sample. They suggest that the spurious signal may be suppressed by carefully aligning the applied magnetic field with the propagation direction of the pump/probe beams, and by improving the polarization purity of optical elements in the experiment. The revised experimental setup is shown in Figure 6.1 (a). After implementing the revised experimental setup, the observed spurious EIT feature width was reduced and inverted, as shown by the blue curve in Figure 6.1 (b).

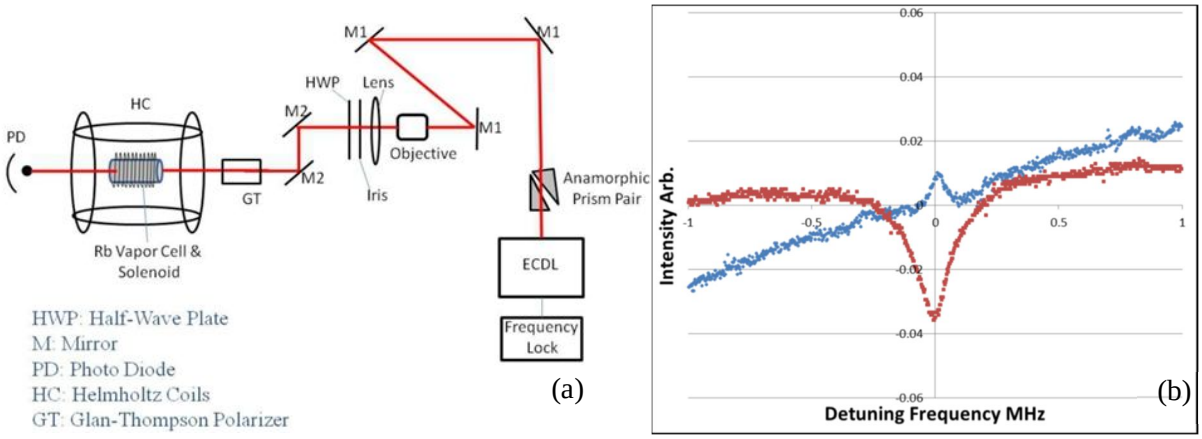

Figure 6.1 Apparatus and associated data from Refs. [49] and [50]. (a) Experimental apparatus. A single linearly polarized beam is incident on a Rb sample gas in a magnetic field, and transmission is observed via photodiode. (b) A quarter wave plate changes the input beam to pure circular polarization, and spurious EIT-like features are observed for different polarization purities. The red trace is taken at purity of 10^3 (i.e., when absorptive polarizers [ThorLabs LPNIRE100-B] are used), and is a large EIT-like spurious feature. The blue trace, at polarization purity 10^5 (i.e., when Glan-Thompson polarizers [Newlight Photonics GPC0210] are used) is much smaller, and inverted.

Seeing the drastic improvement in the spurious feature, we considered that the spurious feature was small enough to justify modifying our experiment to use separate circularly polarized pump and probe beams, as discussed in the next section. After the modification, we note conditions under which the large spurious feature of Figure 6.1(b) returns.

7. Separate circularly polarized pump and probe: Effect of relative angle

We investigate the effect of small and large relative pump/probe angle on beam transmission. To do this, we modify our apparatus to allow for separate control of pump and probe beams. We consider the effect of relative pump/probe angle on observed feature lineshape, and discuss relative pump/probe angle in the context of Dicke narrowing in EIT.

7.1. Apparatus for separate circularly polarized pump and probe beams

We made changes to the apparatus of Figure 6.1 to enable separate control of the pump and probe intensities as shown in Figure 7.1 in order to systematically investigate the effects of misalignment of the pump and probe fields with the applied magnetic field. Preliminary results comparing the effects of small and large relative angles between pump and probe are indicated in Figure 7.2.

Separate control over the pump and probe beams in a Zeeman configuration is attained by separating the single linearly polarized beam into two beams of orthogonal linear polarizations. These beams may be independently frequency-shifted and intensity-adjusted as desired, and re-combined before conversion to circular polarization. This separation and recombination of the pump and probe beams introduces some finite angular separation between the two beams. Similar angular separation also exists in traditional EIT/EIA.

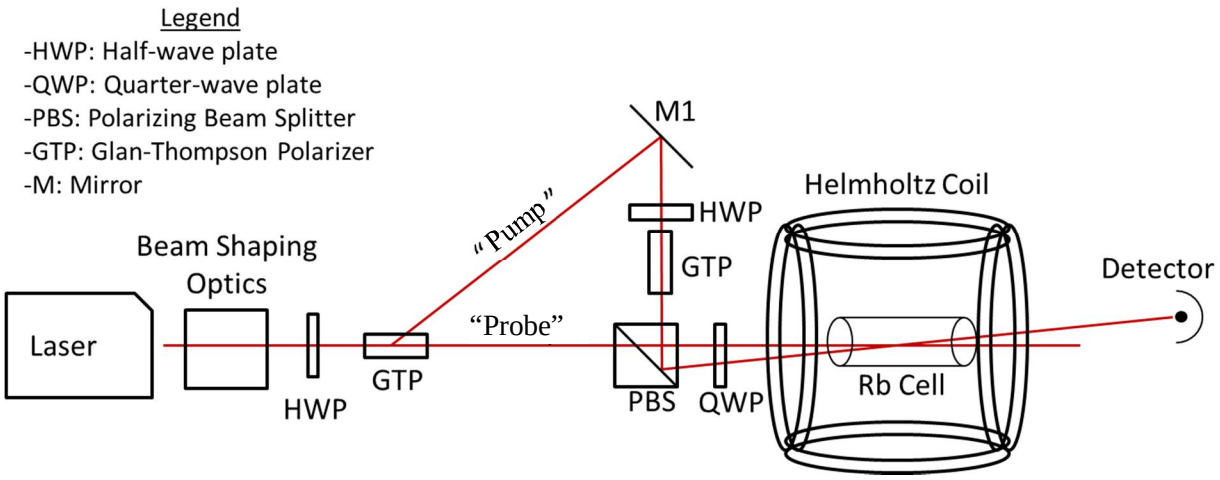

Figure 7.1 Experimental apparatus used in [50]. Orthogonal linearly polarized pump and probe beams are separately intensity controlled by half wave plates and Glan Thompson polarizers, recombined at a polarizing beamsplitter, and converted to right- and left- circular polarization. Note that we may align either the pump or the probe beam onto the detector.

7.2. Experimental Procedure

Working with this experimental apparatus, we observed a similar spurious EIT like feature to the red trace of Figure 6.1 (b) *when the probe beam was blocked*, as seen in Figure 7.2 (b). We suspected that that the spurious EIT-like feature persisted in the pump transmission spectra due to the angle between the pump's propagation direction and the magnetic field, and was eliminated in the probe transmission spectra because this angle was minimized. We then adjusted the pump propagation direction to form an angle of 0.66 milliradians (0.04°) with the probe propagation direction such that the pump & probe field intersected within the Rb vapor cell, and observed the EIT feature at different pump and probe intensities. After the adjustments, we saw that the spurious feature was again suppressed and inverted (similar to the blue trace of

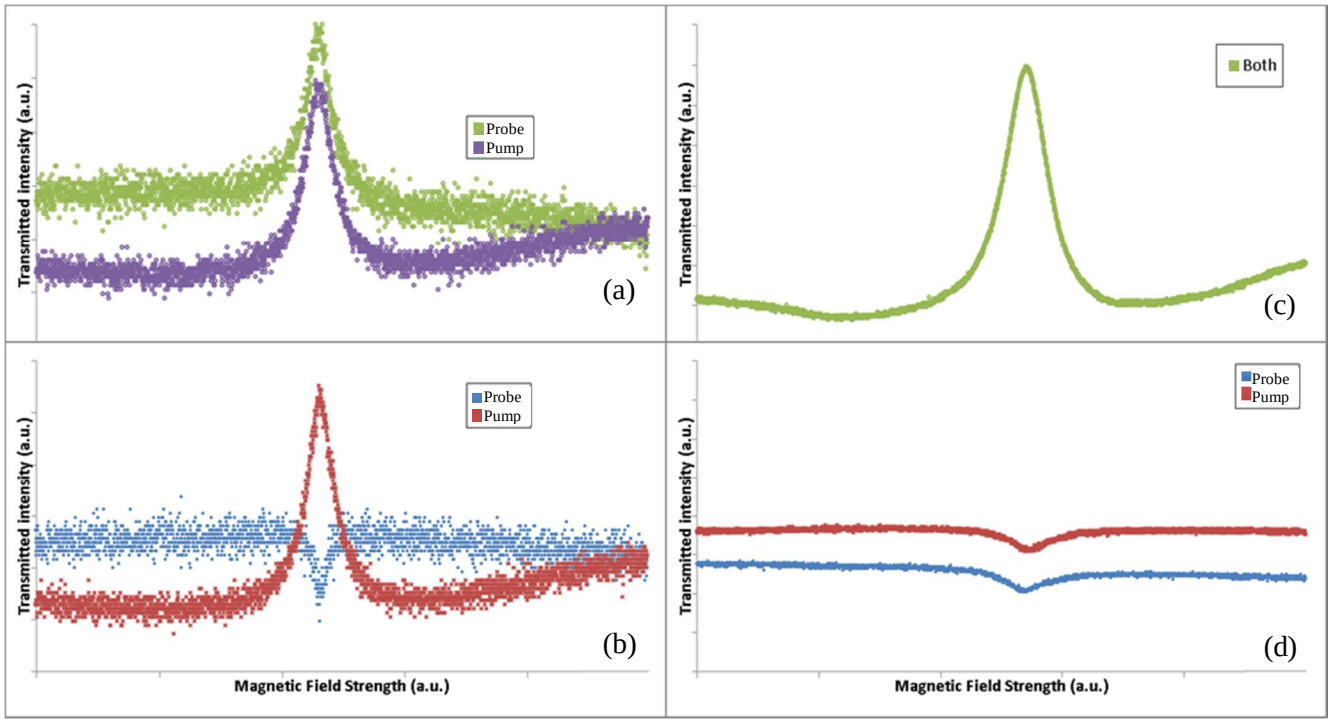

Figure 7.2 Pump and probe transmission spectra are observed on separate detectors. (a) EIT-like features observed at large relative angle (θ=3.8 milliradians) with powers P_{pump}=1.22μW and P_{probe}=0.17μW. (b) Features observed for individually incident pump and probe beams at large relative angle; the spurious feature in the probe is suppressed and inverted suggesting that the probe feature seen in (a) is genuine. However, the pump feature seen in (a) is unchanged in (b) when the probe is blocked. Hence, the pump features in (a) and (b) are entirely spurious. (c) EIT feature for co-incident pump and probe at small relative angle (θ=0.7 milliradians) with powers P_{pump}=74 μW and P_{probe}=70 μW. Note that we were unable to separate the pump and probe for individual observation due to the small angle between the two beams. (d) Spurious features for individually incident pump and probe beams at small relative angle; the spurious EIT-like feature is strongly suppressed and inverted in both the pump and probe measurements, indicating that the EIT feature seen in (c) is genuine.

Figure 6.1(b)) compared to the two-beam EIT feature, as shown in Figure 7.2(c) and (d). We took data for both pump and probe beam (together and individually) for three different angles (0.66, 1.65, and 3.82 milliradians), and at four different intensities (90, 60, 35, and 10uW. In each case, $I_{pump} \approx I_{probe}$). We found that the spurious EIT-like signal returned when the angle was adjusted to 3.8 milliradians; representative measurements for large angles are shown in Figure 7.2 (a) and (c).

7.3. Comparison of large and small relative pump/probe angles

For all measurements shown in Figure 7.2, the pump and probe transmission spectra are observed on two separate detectors. The measurements taken at large relative pump/probe angle are on the left (Figure 7.2(a) and (b)), and the measurements taken at small relative pump/probe angle are on the right (Figure 7.2(c) and (d)). In the measurements on the top (Figure 7.2(a) and (c)), the pump and probe beams are both incident on the sample, whereas in the bottom measurements (Figure 7.2(b) and (d)), only one of the two beams is incident on the sample, and the other is blocked.

7.3.1. Large relative pump/probe angle

When the pump is blocked, the probe feature (blue curve in Figure 7.2(b)) is small and inverted compared to when both beams are incident on the sample (green curve in Figure 7.2(a)). However, when the probe is blocked, the pump feature (red curve in Figure 7.2(b)) is the same as when both beams are incident on the sample (purple curve in Figure 7.2(a)); this indicates that, although the observed spectrum resembles an EIT feature, it is entirely spurious.

7.3.2. Small relative pump/probe angle

When only one of the pump or probe beams is incident on the sample, the resulting features (red and blue curves in Figure 7.2(d)) are small and inverted compared to the feature observed when both beams are incident on the sample (green curve in Figure 7.2 (c)); this indicates that the observed EIT feature is genuine.

In the next section, we consider the effect that relative pump/probe angle has on the effective polarization of the light, and on the Doppler shifts of pump/probe photons as observed by a sample atom.

7.4. Analysis of results: relative angle consideration

We consider two principal sources of change in the lineshape of the observed EIT/EIA features with varying pump/probe angle: magnetic field alignment and differences in Doppler shift.

First, a finite pump/probe angle necessitates that at least one of the two beams is not collinear with the applied magnetic field. Accordingly, that beam is observed by the atom as slightly elliptically polarized; the linear component of the elliptically polarized beam can itself be viewed by the atoms as a superposition of left and right circularly polarized light, yielding its own (spurious) EIT/EIA features. This explains the pump-only trace in Figure 7.2, wherein the large angle between the pump beam and the magnetic field introduces elliptically polarized light, causing an EIT feature even in the absence of the probe field. Without restricting the relative pump probe angle to zero, there is really no way to entirely avoid this problem.

Second, a moving atom sees a Doppler shift in the pump frequency that is different from the Doppler shift in the probe frequency. Given pump and probe photons with the same frequency, and assuming the atomic velocity v to be aligned with the pump propagation direction, the Doppler-shifted pump frequency seen by the atom is given by $f_{pump} = (1 + v/c)f_0$. However, for the probe photon incident on the same atom at some angle θ, the Doppler-shifted probe frequency seen by the atom is $f_{probe} = (1 + vcos(\theta)/c)f_0$. As these pump and probe photons are effectively different frequencies, the probability amplitudes associated with the desired transitions are no longer equal, and the overall EIT/EIA feature amplitude is decreased.

In the next section, we discuss one elegant method for suppressing Doppler shift mismatch.

7.5. Dicke narrowing

One method of minimizing atomic velocity in order to suppress the above-mentioned Doppler mismatch between pump and probe frequencies seen by the atom is to introduce a buffer gas into the sample. When sample atoms collide with the buffer gas atoms, their velocity v changes, but their internal state does not.

In order to define a Doppler shift the atom must travel at least a distance equal to an optical wavelength λ. However, with the introduction of a buffer gas, if the collision rate γ between Rb atoms and buffer gas atoms becomes sufficiently high, the mean free path $\Lambda = v/\gamma$

may become comparable to or smaller than λ. In that case, the average velocity of the atom approaches zero, such that the atom observes no Doppler shift. This reduction in Doppler broadening due to velocity-changing collisions with buffer gas atoms is referred to as Dicke narrowing.

Ref. [39] shows that, in addition to reducing the Doppler broadening of absorptive features, Dicke narrowing can also be seen in coherent population trapping (CPT) resonances such as EIT. Ref. [39] goes on to derive an expression for a Dicke narrowed CPT resonance spectrum with residual Doppler broadening:

$$S_2(\Delta_R) = \frac{-|\Omega_2|^2}{(\Gamma_1+\eta\Gamma_D)^2}\frac{\Gamma_{12}+\eta\Gamma_D^{res}}{\Delta_R^2+\left(\Gamma_{12}+\eta\Gamma_D^{res}\right)^2} \quad (12)$$

Here, $\Delta_R = \omega_1 - \omega_{21} - \omega_2$ is the Raman detuning, ω_1 and ω_2 are the respective pump and probe frequencies, ω_{21} is the energy difference between the ground states, Ω_2 is the Rabi frequency of the strong pump beam, Γ_1 is the relaxation rate from the excited state to a ground state, $\Gamma_D = q_1 v$ is the Doppler width, q_1 and q_2 are the pump and probe wave vectors (in the direction of beam propagation), Γ_{12} is the inherent width of the CPT transition (Ref. [39]), and $\Gamma_D^{res} = |q_1 - q_2|v$ is the residual Doppler width.

For CPT resonances with two beams, a Dicke narrowing factor η may be defined, which depends on a comparison of λ_{CPT} (defined as$2\pi/|q_1 - q_2|$) and the mean free path of the atom Λ:

$$\eta \equiv \Lambda|q_1 - q_2| = 2\pi\frac{\Lambda}{\lambda_{CPT}} \quad (13)$$

Following this theory, Ref. [26] explicitly includes the pump/probe angle term into the CPT lineshape of Eq. (12) in the specific context of EIT, for small angles. To do this, the authors approximates (in Ref. [26]) that, for $\theta \leq 1$ milliradian and $|q_1| = |q_2| = q$, it is reasonable to assume $|q_1 - q_2| = q\theta$. Thus, the Dicke narrowing factor becomes

$$\eta = \Lambda|q_1 - q_2| = q\theta\Lambda = 2\pi\theta\frac{\Lambda}{\lambda_{EIT}} \quad (14)$$

With this change, we plug η into Eq. (1), and obtain the EIT resonance spectrum, correcting a typographical error in the final result of Ref. [26]:

$$S_2 = \frac{-|\Omega_2|^2}{(\Gamma_1+(2\pi\Lambda/\lambda_{EIT})\theta\Gamma_D)^2}\frac{\Gamma_{12}+(2\pi\Lambda/\lambda_{EIT})\Gamma_D\theta^2}{\Delta_R^2+(\Gamma_{12}+(2\pi\Lambda/\lambda_{EIT})\Gamma_D\theta^2)^2} \quad (15)$$

So, the Dicke narrowed width of the feature has become

$$\eta\Gamma_D^{res} = (2\pi\Lambda/\lambda_{EIT})\Gamma_D\theta^2 \quad (16)$$

indicating a quadratic dependence of the Dicke-narrowed Doppler width on pump/probe angle.

In the next chapter, we re-construct our apparatus after moving to a new building. We also make improvements to the apparatus to enable us to obtain EIT/EIA spectra as a function of relative pump/probe angle in a standard Rb cell. In the subsequent chapters, we discuss improvements to the apparatus as a precursor to our own study of the effect of relative pump/probe angle in a Rb vapor cell containing buffer gas.

8. Improvement to our Experimental Apparatus

After performing the measurements of the Chapter 7, we completely deconstructed our apparatus to prepare to move to a new building. After the move, we re-constructed the apparatus and made improvements to a) improve the spatial mode of the laser beams by coupling the laser through a single-mode optical fiber, b) improve the frequency stability of the laser source by inserting an optical isolator, and c) improve the magnetic field homogeneity inside the sample by employing a well-constructed solenoid.

In this chapter, we discuss a) and b) above. We utilize our improved apparatus to obtain EIT/EIA data with separate circularly polarized pump and probe beams, and study the effect of different probe intensities on the observed EIT/EIA spectra

8.1. Experimental Apparatus

The new generation experimental apparatus is shown in Figure 8.1. In this apparatus, an external cavity diode laser (ECDL) is tuned to resonance with the ^{85}Rb D2 line via Saturated Absorption Spectroscopy (SAS). The elliptical beam from the ECDL is circularized using an anamorphic prism pair to aid in uniform coupling into a single-mode fiber optic cable. The output of the single-mode fiber is a clean Gaussian beam with FWHM of 0.4mm. This beam is

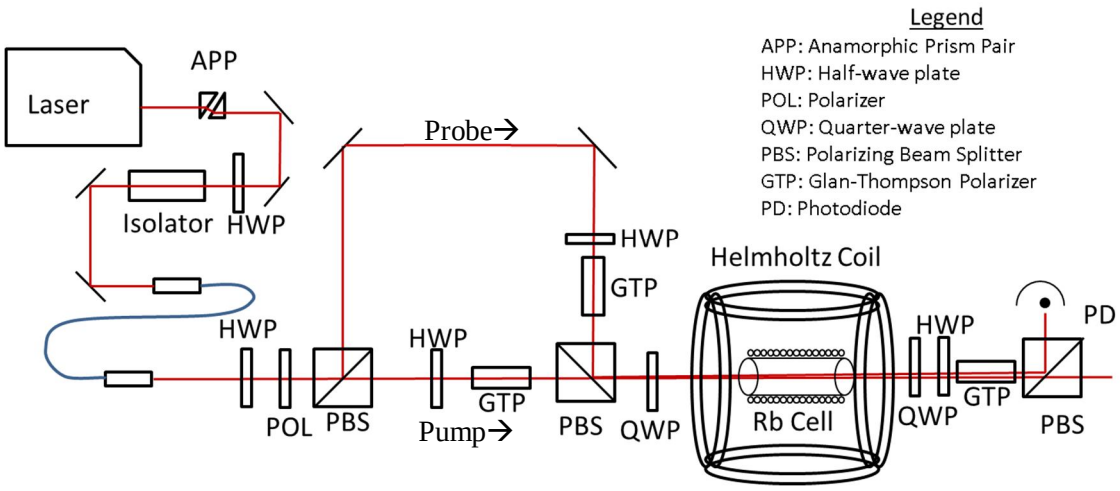

Figure 8.1 Experimental apparatus for preliminary observation of EIT/EIA. A beam from an external cavity diode laser is guided through a fiber optic cable to a polarizing beam splitter. This beam is split into $\pi \perp \pi$ pump and probe beams, whose intensities are adjusted by Glan-Thompson polarizers. After recombining, the beams are converted to left and right circular polarization, and pass through a Rb vapor cell wrapped with a solenoid. Transmitted probe intensity is observed on a photodiode.

evenly divided by a polarizing beamsplitter into orthogonal linearly polarized pump and probe beams, intensity-adjusted by half wave plates and Glan-Thompson polarizers, and re-combined at second a polarizing beamsplitter. The re-combined beams are then passed through a quarter wave plate, which yields orthogonally circularly polarized pump and probe beams. These beams are allowed to be incident on the Rb sample inside a solenoid-wrapped vapor cell shown in Figure 8.2. We persisted with this solenoid design for initial measurements, but converted to a far better design in the measurements of Chapter 9.

After transmission through the Rb vapor, the circularly polarized beams are converted back to linear polarization via a second quarter wave plate. A half-wave plate and Glan-Thompson polarizer are set to minimize the pump beam transmission. A polarizing beam splitter directs the probe beam toward a photodiode, and again serves to minimize the pump power incident on the photodiode. The Glan-Thompson polarizer and half wave plate greatly suppress, but do not entirely eliminate, the pump leaking through to the photodiode, as seen in Chapter 8.6.2.

8.2. Intensity measurement

In order to determine the intensity of the pump and probe beams respectively, it is necessary to determine the spot size of each beam; however, the beams are too small for the radius to be determined accurately via direct measurement. To determine the radius, we used the apparatus shown in Figure 8.3 to magnify the beam. This enabled us to make an accurate measurement of the spot size, using $r_o/f = y/d$ where $r_0$is the radius of the input beam, $f$is the

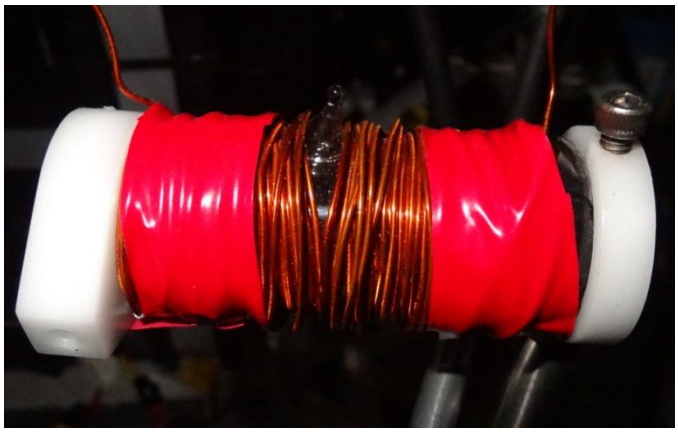

Figure 8.2 A copper wire solenoid wrapped directly around a standard Rb vapor cell. Two Teflon mounts provide boundaries for the wire, and electrical tape prevents the wire from unwinding. The magnetic field at the center of the solenoid is calculated to be 22.7 Gauss/Amp.

focal length of the lens, y is the radius of the spot on the screen, and d is the distance from the focal point to the screen.

The diameter of the Gaussian beam used in our experiment can be described by using the FWHM of the beam's spatial power distribution. In order to determine this spatial power distribution, we installed a movable pinhole directly in front of the screen, and attached the probe of our handheld power meter behind the pinhole. We adjusted the height of the pinhole to find the maximum power in the vertical direction; by finding the maximum power in the vertical direction, we ensure that motion of the pinhole in the horizontal direction will pass through the center point of the Gaussian. We locked the vertical height of the pinhole and varied its horizontal position to locate the positions at which we observed the maximum and half-maximum beam powers. This FWHM is the spot size as observed on the screen, which can then be used to calculate the original spot size to high precision. For our experiment, we calculate a beam radius of 0.43mm.

The handheld power meter used to determine the beam power does not discriminate between beam power inside and outside of the FWHM. Therefore, in order to determine the intensity of the beam within the FWHM, it is necessary to calculate the percentage of the measured power which falls within this region.

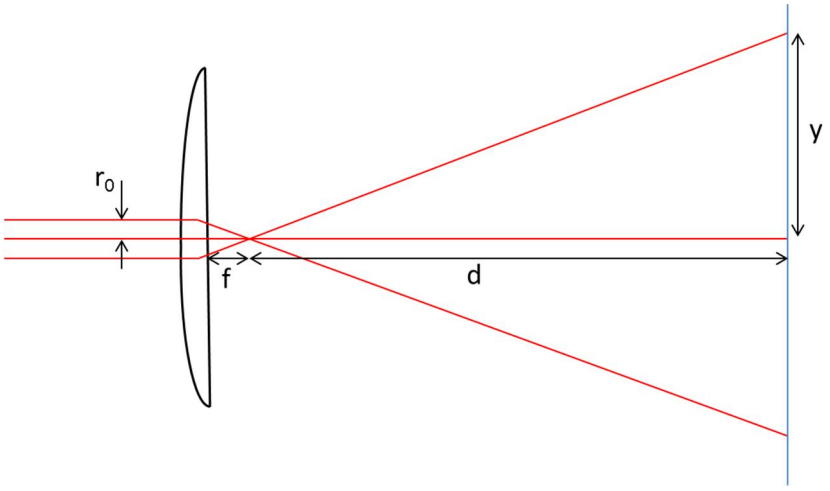

Figure 8.3 Apparatus for spot-size measurement. A beam of interest is magnified by a lens, and the divergent beam is viewed on a screen at a known distance from the focal point. By measuring the size of the magnified spot on the screen, the radius r_0 of the original beam can be calculated to good precision.

We start with a normalized 1-dimensional Gaussian,

$$f(x) = \frac{1}{\sigma\sqrt{2\pi}} e^{-\frac{(x-\mu)^2}{2\sigma^2}} \tag{17}$$

where σ is the standard deviation, x is the radial position, and μ is the offset. The FWHM of a Gaussian is commonly known to be $2\sqrt{ln(2)}\sigma$. To get the percentage of the function which falls within this region, we set integrate $f(x)$ over the FWHM

$$\int_{-\sqrt{2ln(2)}\sigma}^{\sqrt{2ln(2)}\sigma} f(x) = \frac{1}{2} erf\left(\frac{x}{\sqrt{2}\sigma}\right)\Big|_{-\sqrt{2ln(2)}\sigma}^{\sqrt{2ln(2)}\sigma} = erf\left(\sqrt{\ln(2)}\right) \approx 76.1\% \tag{18}$$

where $erf(z)$ is the error function. Thus, for a 1D Gaussian, the area under the FWHM constitutes 76.1% of the total area.

Our beam profile is a 2D Gaussian, so we square the result to obtain 58%. Thus, the actual power within the FWHM is only 58% of the total power carried by the Gaussian beam, and accordingly only 58% of the power measured by our handheld power meter.

8.3. Optical Isolator

The requirement to align the single-mode fiber generates strong retroreflections which can cause unwanted feedback in the ECDL. These retroreflections can be suppressed only with the help of a high-quality optical isolator. Accordingly, we installed an optical isolator (Figure 8.4) before the fiber optic cable.

This optical isolator consists of a Faraday rotator between two polarizers set at 45° from one another. In the forward direction, light is set to one polarization by the first polarizer, its polarization is rotated clockwise by 45°, before passing through the second polarizer unaffected.

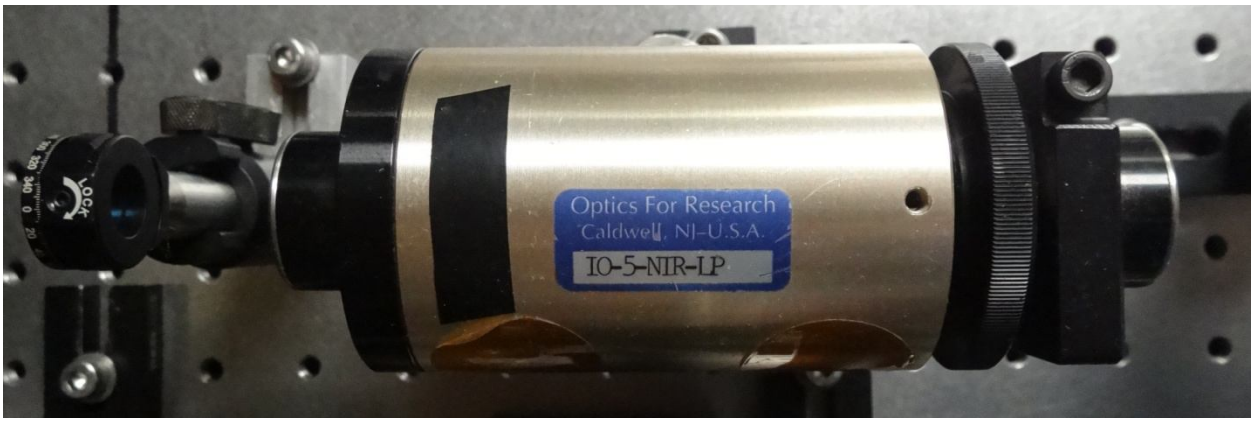

Figure 8.4 Optical Isolator for preventing retro reflections from feeding back into the ECDL.

In the reverse direction, light passes through the second polarizer and its polarization is again rotated clockwise by 45°, so that it is now 90° from the first polarizer, yielding nearly complete attenuation.

To measure the degree of optical isolation provided, we first aligned the beam through the isolator in the forward direction. We then rotated the isolator in place by 180° and re-aligned the beam in the reverse direction to maximize throughput. We slightly adjusted the angle of the second polarizer to reduce the throughput in the reverse direction, and recorded the beam power before and after the isolator (25.34 mW and 2.2 μW, respectively). We rotated the isolator back to the forward direction and again recorded the beam power after the isolator (20.85 mW).

This procedure optimizes the extinction in the reverse direction, maximizing the attained isolation. This gives an extinction of ($10\log_{10}(20.85\text{mW}/2.2\text{uW})=-39.8\text{dB}$), which compares favorably with the extinction stated in the documentation, -40.5dB. This high degree of isolation is sufficient to protect the ECDL from the retroreflections coming from the input lens coupler to the optical fiber.

8.4. Calibration of Linewidth of spectral features for Scanning magnetic field Zeeman EIT/EIA

First, we cancel out the ambient magnetic field using a Helmholtz coil. The magnetic field at the center of the Helmholtz coil was measured using a Gauss/Tesla Meter (Sypris 7030). The Z-direction of a 3-axis probe was aligned with the intended beam propagation direction, and the x-direction was set parallel to the optics table. With the probe in position, a magnetic shield called a “zero-flux chamber” was attached to the end of the probe, and the instrument was zeroed.

The zero flux chamber was removed, and the ambient magnetic field was observed on the gauss meter. DC power supplies driving the x-, y-, and z-direction Helmholtz coils were then adjusted to reduce the DC magnetic field to the order of 5 milliGauss or less in each direction. This completes the rough zeroing of the ambient magnetic field within the Helmholtz coils.

After rough zeroing is complete, the Rb vapor cell and solenoid are installed within the Helmholtz coil, and an EIT/EIA feature is observed on the oscilloscope. It is shown in Ref. [50] that transverse magnetic fields induce a broadening of the observed EIT/EIA feature, and accordingly we set the transverse magnetic fields to attempt to minimize the observed FWHM of the EIT feature. This completes the fine zeroing of the magnetic field.

Probe absorption is observed while scanning the magnetic field through the cell via a solenoid. We record the generated EIT/EIA features on an oscilloscope, as shown for example in Figure 8.5. In order to measure the spectral linewidths of the EIT/EIA features, it is necessary to calibrate the horizontal oscilloscope scale in terms of the magnetic field scan rate.

The magnetic field (in Tesla) in the center of the solenoid can be calculated using

$$B = \frac{\mu_0 NI}{\sqrt{L^2+4R^2}} \tag{19}$$

where μ_0 is the magnetic permittivity of free space, N is the number of turns in the solenoid, we is the current, L is the length of the solenoid, and R is the radius of the solenoid. For the solenoid of Figure 8.2, N = 121, L = 60.7 mm, and R = 13.35 mm, giving a magnetic field of 22.9 Gauss per Ampere.

The current through the solenoid at a given time is observable via a dedicated 1 A/1.06 V-scaled current monitor, which is recorded in each oscilloscope output. By determining how many seconds the measured feature spans on the oscilloscope, the current through which the solenoid has been scanned can be determined and converted to a difference in magnetic field in Gauss.

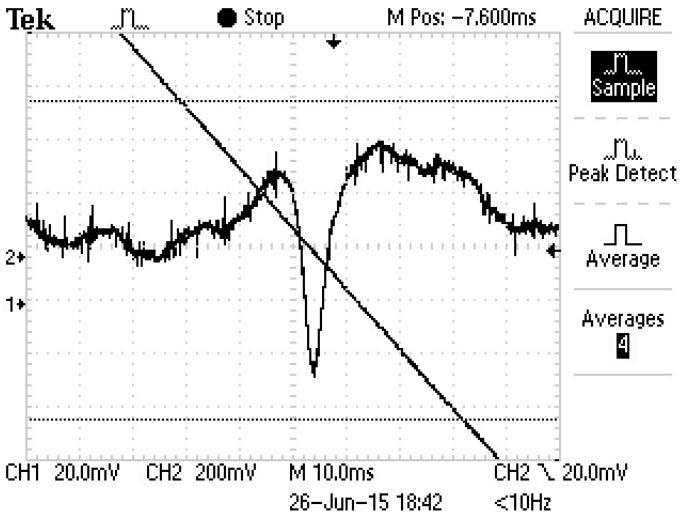

Figure 8.5 Example oscilloscope trace taken for ^{85}Rb F_g=2 →F_e=1, 2, 3 showing an EIT feature. The magnetic field scan rate is given by the slope of the diagonal line; this scan rate is needed to calibrate the width of the feature in Gauss (or in MHz if the Zeeman splitting is known), enabling calculation of the feature's FWHM.

8.5. Procedure

The ECDL is tuned to resonance with a desired transition within the D2 line of either ^{87}Rb or ^{85}Rb via Saturated Absorption Spectroscopy. The power of each beam is measured before the Rb sample cell. The intensities of the pump and probe beams are independently varied by rotating a half-wave plate before the relevant Glan-Thompson polarizer (see pump and probe paths in Figure 8.1). For each of three different probe intensities, EIT/EIA features and associated spurious features are observed on an oscilloscope. The frequency of the two beams is slightly adjusted to optimize the EIT or EIA feature and to reverse gradual drift of the laser frequency. The frequency of this optimum position is recorded to improve repeatability of measurement.

The pump power is held fixed for all measurements at about 85μW (8.73 I_{sat}, χ =12.68 MHz) and the probe powers were varied between 0.34and 1.35μW (0.035 to 0.140 I_{sat}, χ =0.8 to 1.6 MHz). These powers were selected for comparison with the Rabi frequencies χ_{pump}=15.7 MHz and χ_{probe}= 0.94 MHz used in Ref. [50].

8.6. Results/Observations for EIT/EIA spectra in the scanning magnetic field configuration

In the observations below, the angle between pump and probe beams for this data is held fixed at 0.26 milliradians. EIT/EIA spectra are measured in the scanning magnetic field configuration for all four D2 ^{85}Rb and ^{87}Rb transition groups described in Chapter 5.3. The final polarizing beamsplitter and Glan-Thompson polarizer in Figure 8.1 are set to transmit only the probe beam to the detector, so all measurements are of the probe transmission spectra only.

For the data given in each of Figure 8.6-Figure 8.9, (a) is the *"EIT"* or *"EIA"* feature, wherein the probe absorption spectrum is shown when both pump and probe beams are incident on the sample. (b) is the "*Pump Spurious*" feature, wherein the probe absorption spectrum is shown when only the pump beam is incident on the sample; since the probe is blocked, any laser light incident on the detector is leakage from the pump. (c) is the *"Probe Spurious"* feature, wherein the probe absorption spectrum is shown when only the probe is incident on the sample; in absence of the pump, the weak probe beam should be entirely attenuated by the Rb vapor. (d) is the *"EIT - Pump Spurious"* or *"EIA - Pump Spurious"* feature, wherein the pump leakage (b) is subtracted from the EIT/EIA feature (a), yielding the true EIT/EIA feature.

8.6.1. EIT Features

The observed ^{85}Rb F_g=2 →F_e=1, 2, 3 EIT features and associated pump and probe spurious features are shown in Figure 8.6, and the observed ^{87}Rb F=1 to F'=0, 1, 2 EIT features and associated pump and probe spurious features are shown in Figure 8.7. For all features, I_{pump} ≈ 8.95 I_{sat} (χ = 12.83 MHz), and I_{probe} ≈ 0.035 I_{sat}, 0.70 I_{sat}, and 0.135 I_{sat} (χ = 830 kHz, 1.13 MHz, and 1.57 MHz, respectively).

The ^{85}Rb F_g=2 →F_e=1, 2, 3 EIT features were measured on the 20mV/division scale. As expected, larger probe power yields a larger EIT feature. Although no probe spurious feature is visible at any of the probe powers, the pump shows a small spurious feature (Figure 8.6(b)) which may affect the observed EIT lineshape. The FWHM for these features in Figure 8.6(d) was measured to be 1.01 G, 1.00 G, and 1.04 G, in order of least-to-greatest probe power, respectively. These features are 2-3 times more broad than the single π–beam EIT features reported by previous researchers in our group [50].

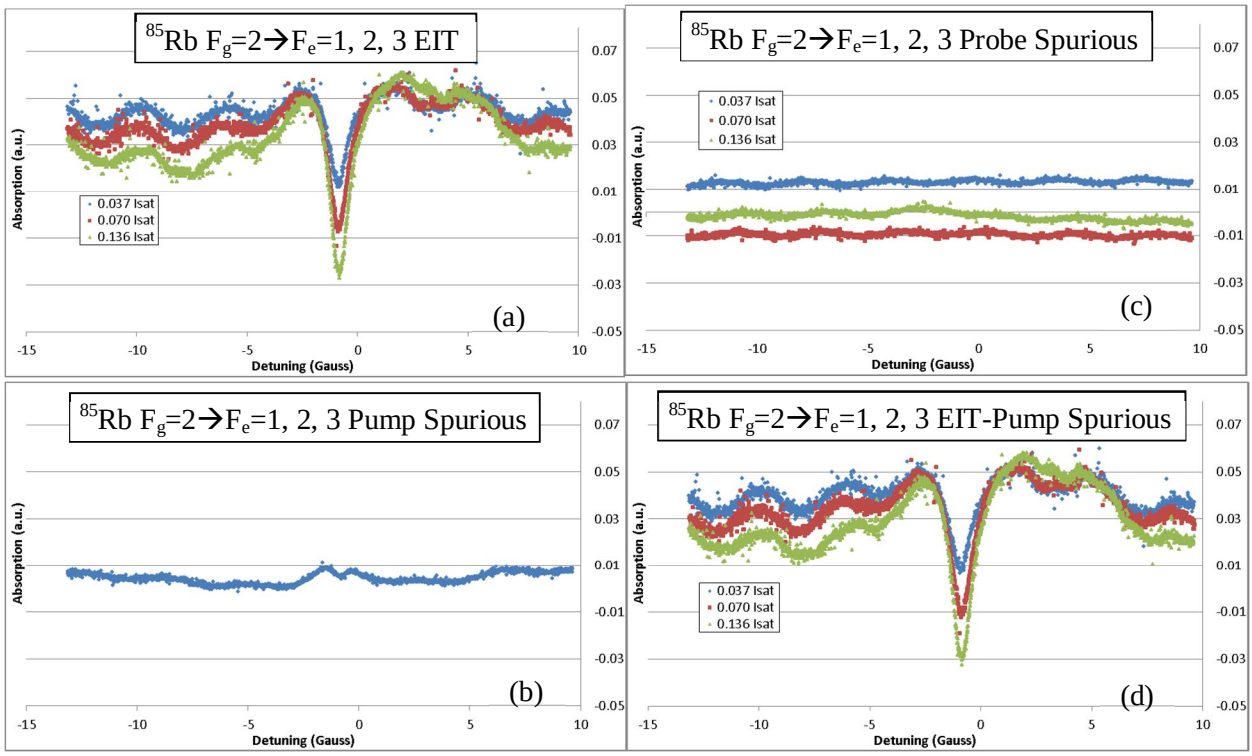

Figure 8.6 Probe absorption spectra for the ^{85}Rb F_g=2 →F_e=1, 2, 3 group of transitions, for which EIT is expected, obtained using the apparatus of Figure 8.1. For these measurements, I_{pump} = 8.95 I_{sat} and I_{probe} = 0.035 I_{sat} (blue), 0.070 I_{sat} (red), and 0.135 I_{sat} (green). The relative angle between pump/probe is fixed at 0.26 milliradians.

The ^{87}Rb F_g=1 →F_e=0, 1, 2 EIT features were small, only visible on the 2mV/division scale on the oscilloscope. The background electrical noise is clearly evident in Figure 8.7, but the EIT features are still visible. Due to the low SNR evident in the data, no meaningful calculation of the FHWM of the actual EIT features can be made; nevertheless, rough calculation places these FWHM at about 1.4-1.7 G.

It is worth noting that, of all of the ^{87}Rb and ^{85}Rb D2-line transitions, the ^{87}Rb F_g=1 →F_e=0 transition is unique in that the F_e=0 excited state does not undergo a Zeeman shift in the presence of a magnetic field; additionally the σ^+ and σ^- pump and probe beams both cause transitions from m=±1 ground states to the m=0 excited state, such that the pump and probe detunings caused by the Zeeman shift are symmetric. Accordingly, for this transition alone, a more reasonable calculation of the EIT feature FWHM in MHz can be performed as described in Chapter 5.4.

The Zeeman shift of the |F_g=1, m=+1> magnetic sublevel is (1)(-70MHz/Gauss) = -70 MHz/Gauss, that of the excited state is 0MHz/Gauss, and that of the |F_g=1, m=-1> is

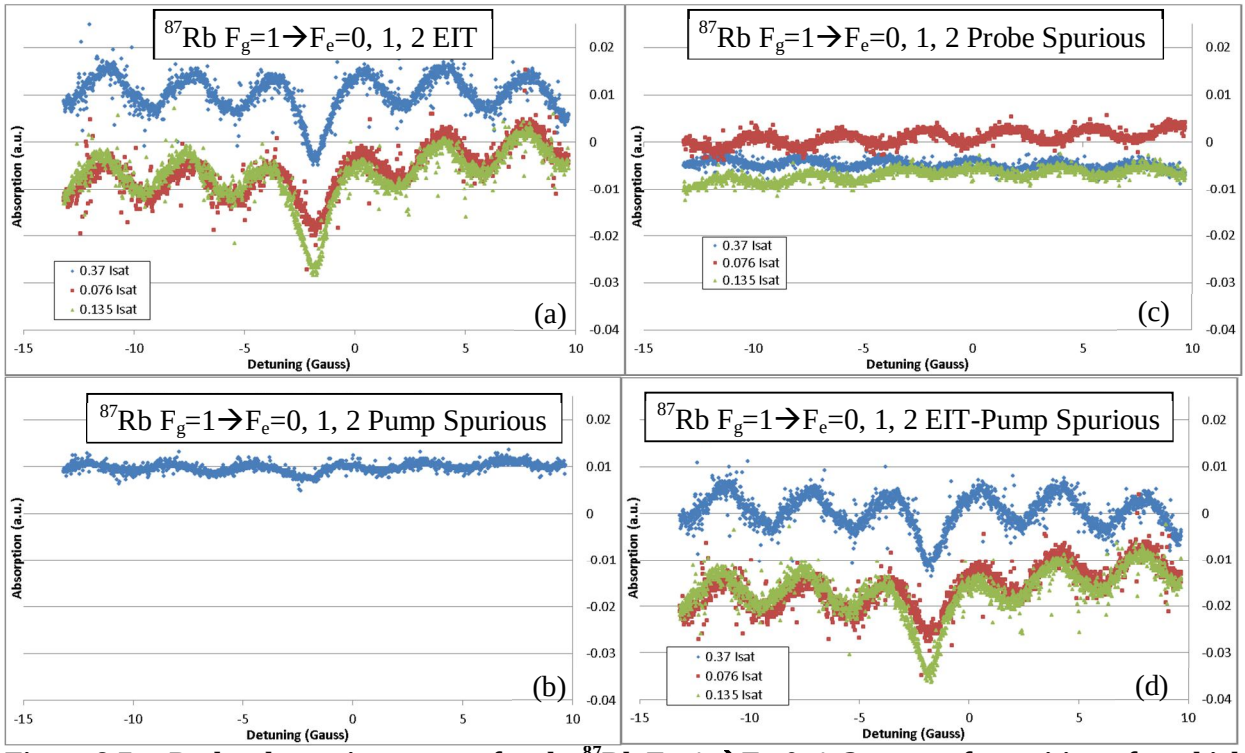

Figure 8.7 Probe absorption spectra for the ^{87}Rb F_g=1 →F_e=0, 1, 2 group of transitions, for which EIT is expected, obtained using the apparatus of Figure 8.1. For these measurements, I_{pump} = 9.13 I_{sat} and I_{probe} = 0.035 I_{sat} (blue), 0.074 I_{sat} (red), and 0.135 I_{sat} (green). The relative angle between pump/probe is fixed at 0.26 milliradians.

(-1) (-70MHz/Gauss) = +70MHz/Gauss. Thus, the net shift between these two levels is 140MHz/Gauss.

For low pump detuning and high pump intensity as is the case in this measurement, the probability amplitude associated with the pump transition is approximately constant. Naively assuming that the probe detuning scans at the whole rate of 140MHz/Gauss, the observed EIT feature FWHM's scale to 1.96-2.38 MHz.

These are on the same order of magnitude as the 3.4MHz obtained in our theoretical consideration of Zeeman EIT for a $|F_g=1\rangle$ to $|F_e=0\rangle$ system, given in Chapter 5.2.

8.6.2. EIA Features

The observed ^{85}Rb $F_g=3 \rightarrow F_e=2, 3, 4$ EIA features and associated pump and probe spurious features are shown in Figure 8.8, and the observed ^{87}Rb $F_g=2 \rightarrow F_e=1, 2, 3$ EIA features and associated pump and probe spurious features are shown in Figure 8.9. For all features, $I_{pump} \approx 8.95\ I_{sat}$, and the measurement is repeated for each of three different probe powers $I_{probe} \approx$

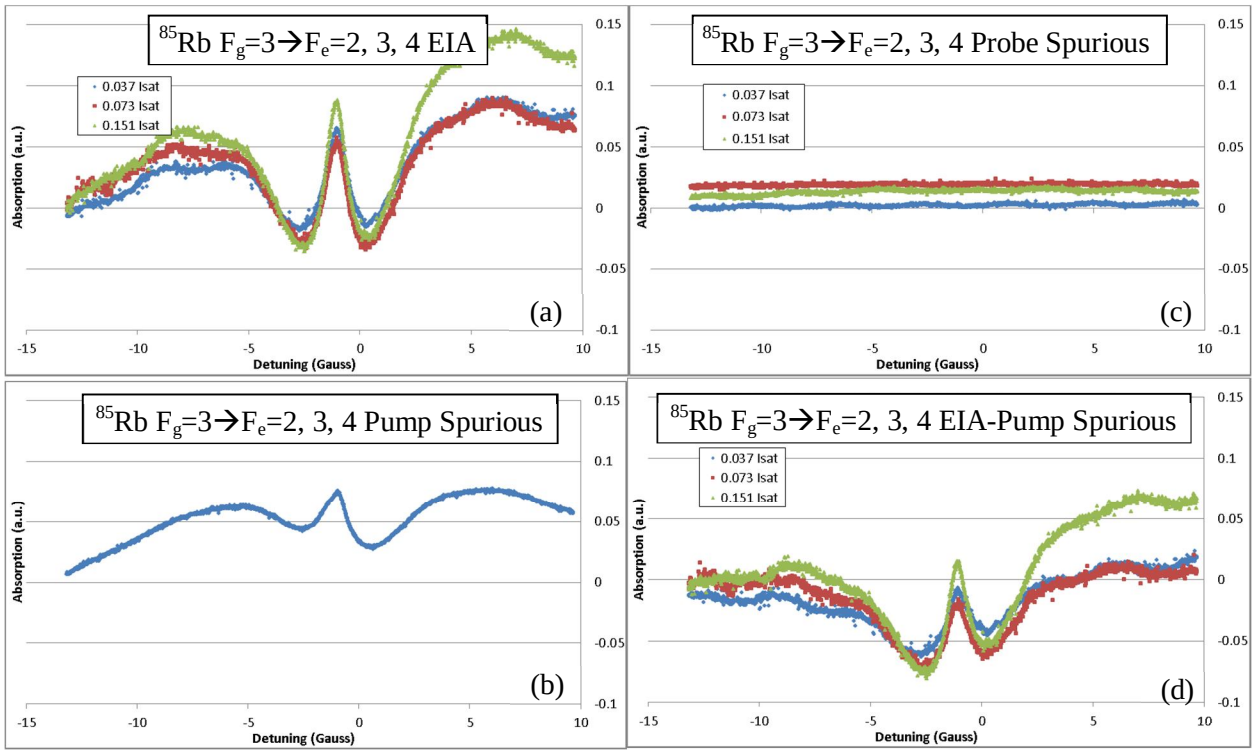

Figure 8.8 Probe absorption spectra for the ^{85}Rb $F_g=3 \rightarrow F_e=2, 3, 4$ EIA spectra observed at $I_{pump} = 9.13\ I_{sat}$ and $I_{probe} = 0.035\ I_{sat}$ (blue), $0.074\ I_{sat}$ (red), and $0.153\ I_{sat}$ (green), using the apparatus shown in Figure 8.1. Relative pump/probe angle is fixed at 0.26 milliradians. (a) Measured EIA feature given as measured probe absorption vs. detuning. (b) Pump spurious feature in absence of the probe beam. (c) Probe spurious features in absence of the pump beam. (d) Difference between the observed EIA and the pump spurious features.

0.035 I_{sat}, 0.074 I_{sat}, and 0.153 I_{sat}.

The ^{85}Rb F_g=3 →F_e=2, 3, 4 EIA features were measured on the 20mV/division scale. Again, larger probe power yields a taller EIA feature; note that the I_{probe} = 0.037 I_{sat} feature in Figure 8.8(a) is slightly offset, making it falsely appear to be taller than the I_{probe} = 0.073 I_{sat} feature. No probe spurious feature is visible at any probe power, Figure 8.8(c). We note that a significant spurious feature is present in the pump-only transmission spectrum (Figure 8.8(b)) even despite use of a Glan-Thompson and polarizing beamsplitter to prevent the pump from leaking through to the photodiode. In order to calculate the FWHM for these features, the pump spurious feature is first subtracted from the EIA feature before measurement. The FWHM for the central absorption spikes in these corrected features was measured to be 1.11 G, 0.91 G, and 0.98 G, in order of least-to-greatest probe power, respectively.

The ^{87}Rb F_g=2 →F_e=1, 2, 3 EIA features were visible on the 10mV/division scale on the oscilloscope. The background electrical noise is evident in Figure 8.9, but the EIT features are

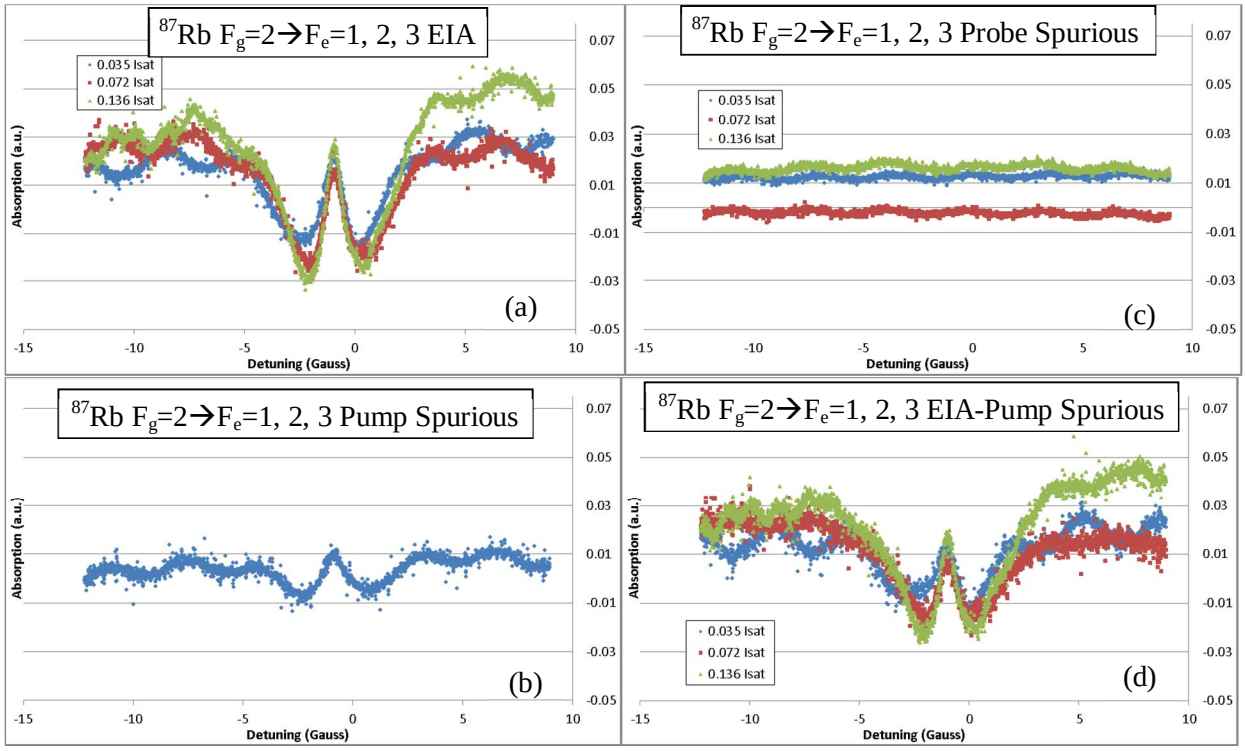

Figure 8.9 Probe absorption spectra for the ^{87}Rb F_g=2 →F_e=1, 2, 3 EIA spectra observed at I_{pump} = 8.97 I_{sat} and I_{probe} = 0.035 I_{sat} (blue), 0.072 I_{sat} (red), and 0.136 I_{sat} (green), using the apparatus shown in Figure 8.1. Relative pump/probe angle is fixed at 0.26 milliradians. (a) Measured EIA feature given as measured probe absorption vs. detuning. (b) Pump spurious feature in absence of the probe beam. (c) Probe spurious features in absence of the pump beam. (d) Difference between the observed EIA feature and the pump spurious feature.

still visible. The SNR for these features is does not appear to be a problem in resolving the ultranarrow EIA features, but the electrical noise impacts the calculated FWHM's. The pump spurious feature is also sizeable compared to the EIA features, so we subtract it from the EIA feature for FWHM calculation. From least to greatest probe power, the calculated FWHM's are 1.44 G, 0.87 G, and 0.78 G, respectively. Although this appears to indicate that higher probe power yields decreased FWHMs, this is most certainly the result of a greater SNR decreasing the electrical noise contribution to observed FWHM.

8.6.3. Other Observations

While performing the measurements of Chapter 8.6.1 and Chapter 8.6.2, it was noted that different pump/probe frequencies near resonance with the intended hyperfine transition yielded drastically different probe absorption spectra, introducing asymmetry or even inducing a switch between EIT and EIA features. For example, for the ^{85}Rb F_g=3 →F_e=2, 3, 4 group of transitions, we normally expect to see an EIA feature. However, at the frequencies indicated by red arrows in Figure 8.10, we instead observe EIT features; at the blue arrows, we see the expected EIA features, and in-between the indicated frequencies, we see an asymmetrical feature. We suspect that the switching was due to the nonuniformity of the axial magnetic field, as this phenomenon was no longer observed after switching to the new solenoid described in Chapter 9.

In order to enable repeatable measurements of probe absorption spectra despite this switching, we chose one frequency at which to lock our laser for the ^{85}Rb F_g=3 →F_e=2, 3, 4 group as indicated by the long blue arrow in Figure 8.10.

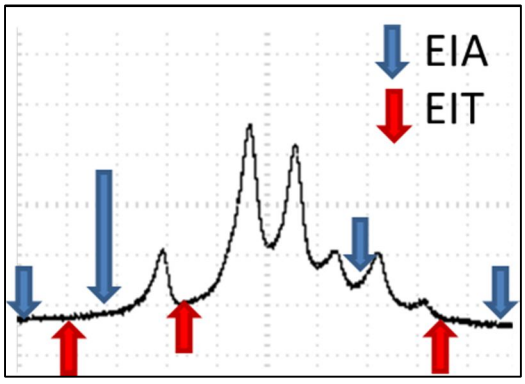

Figure 8.10 Slightly different pump/probe frequencies introduced asymmetry or sign reversal. Laser frequencies at which EIA and EIT were observed are indicated by blue and red arrows on an ^{85}Rb F_g=3 →F_e=2, 3, 4 saturated absorption spectrum with width of 180MHz. Between the indicated points, an asymmetry is observed. The long blue arrow indicates the frequency used in Chapter 8.6.2.

Similar frequency dependent EIT/EIA switching was also observed for ^{85}Rb F_g=2 →F_e=1, 2, 3, for ^{87}Rb F_g=1 →F_e=0, 1, 2, and for ^{87}Rb F_g=2 →F_e=1, 2, 3. To improve repeatability of measurements, the laser was tuned to the blue of each spectrum. These frequencies were easily/repeatably obtainable because they produced the optimum EIT/EIA spectra.

8.7. Conclusions

The calculated FWHM's of the observed features are significantly broader than those reported by previous researchers in our group using a single π–beam Zeeman EIT scheme [50] and [51]. Our observed FWHM's are likely broadened relative to Refs. [41] and [43] by electrical noise and misalignment of the pump beam with the applied magnetic field.

The presence of the spurious pump feature observed in Chapter 8.6.2, despite the use of polarizers to eliminate pump incidence on the photodiode, is directly related to the pump power used in the experiment. Considering the extinction ratio of the Glan-Thompson polarizer, we expect to see on the order of 0.05% of the initial 200uW of pump power leak through to the photodiode; this leakage is comparable to the pump input power of 0.8-3.1uW. In order to reduce the effect of this pump leakage, the pump power was reduced in the measurements of Figure 9.8 (a) and Figure 9.9(a).

The contribution from electrical noise is addressed in Chapter 9.3.

The pump misalignment arises from two different sources: 1) the solenoid used in this experiment does not generate a uniform magnetic field along the cell axis due to the non-uniformity of its wrapping, and 2) the pump beam propagation direction was not adjustable independently from the probe beam. To address the first source, a new, uniformly-wrapped solenoid is installed in Chapter 9.2. To address the second point, additional mirrors allow for control of the pump beam propagation direction in Chapter 9.1.

We note that, with this experimental apparatus and the same pump and probe intensities as Ref. [50], we were able to observe ultranarrow EIA absorption features centered within broad regions of decreased absorption. Using a scanning magnetic field Zeeman configuration, the authors of Ref. [50] were not able to experimentally observe the ultranarrow EIA feature. The authors of Ref. [50] consider that their two separate laser sources each have a linewidth of ~1MHz, giving a 2MHz linewidth difference, i.e., much broader than the ultranarrow EIA feature. We consider that the ultranarrow feature is not observed in their results due to the angle

between the pump and probe beam propagation directions in their experiment, which must be at least large enough to physically separate the pump and probe beams.

Thus, we were able to observe EIT/EIA features on the re-constructed experimental apparatus, and confirmed that the apparatus is functioning properly. We concluded this preliminary experiment, and made further improvements to the experiment as described in the next chapter for the purpose of studying the effect of relative pump/probe angle on EIT/EIA features.

9. EIT/EIA for scanning magnetic field configuration as a function of relative pump/probe angle

In this chapter, we investigate the dependence of EIT & EIA spectral features on the relative angle between the pump and probe beams. To facilitate these measurements, we use a new solenoid for improved magnetic field uniformity.

9.1. Experimental Apparatus

The apparatus used for this experiment is identical to the apparatus of Figure 8.1, with two changes. The main change is the replacement of the solenoid of Figure 8.2 with the solenoid described in Chapter 9.2 to improve magnetic field uniformity and facilitate interchanging between the standard Rb vapor cell used thus far and a Rb vapor cell, containing buffer gas, of different dimensions. The other change is the addition of a lens immediately before the final photodiode, which focusses the transmitted probe beam directly onto the photodiode; this enables us to observe the probe transmission spectra at a small range of probe angles without needing to move the photodiode manually.

9.2. Homogeneous magnetic field with new solenoid

9.2.1. Design

In order to facilitate interchanging a standard Rb vapor cell and a buffer gas cell (shown in Figure 9.1) that have different physical dimensions, we designed two sets of Rb vapor cell holders for repeatably positioning each of the Rb vapor cells in the center of a solenoid wrapped around a form, hereafter referred to as the "solenoid tube", mounted to the optical table.

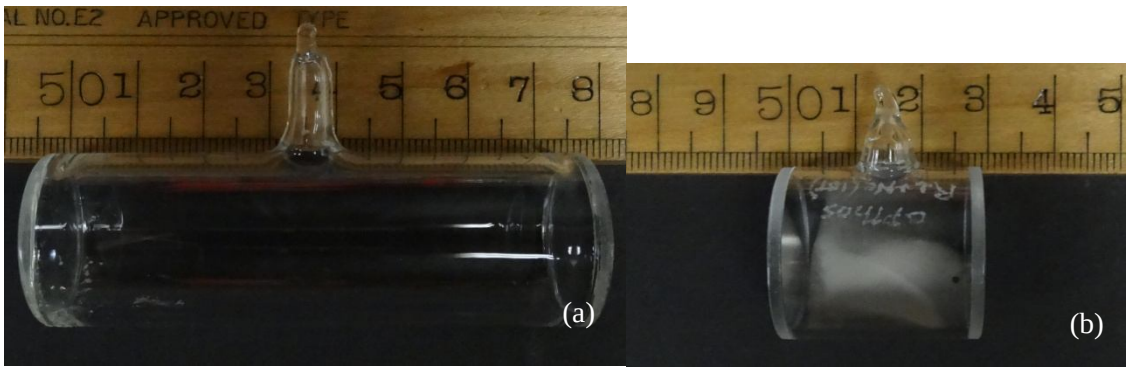

Figure 9.1 Different sizes of Rb vapor cells for use in our experiment. (a) Standard Rb vapor cell containing a natural abundance of ^{85}Rb (72%) and ^{87}Rb (28%) atoms. The cell is measured to be 70.4mm long. (b) Rb vapor cell containing a natural abundance of ^{85}Rb and ^{87}Rb, and 10Torr of Ne buffer gas. The cell is measured to be 28.4mm long.

A CAD rendering of the "standard" holder, the standard Rb vapor cell, and the solenoid tube is shown in Figure 9.2. For CAD drawings of the standard holder, the buffer gas holder, and the solenoid tube including dimensions, see Appendix. The standard holder has a cell-contacting hole on the "inside" end into which our standard Rb gas cell fits snugly. The depth of this hole is such that one end of the Rb vapor cell abuts the end of the hole, thereby preventing a finger on the Rb vapor cell from contacting the end of the holder. This protects the finger from potential damage, and also helps ensure that the cell will remain in the center of the assembly. A smaller diameter hole continues through the rest of the part, providing optical access to the window of the Rb vapor cell on this end. Near the "inside" end of the holder, there is a set screw for locking the Rb vapor cell in place, preventing motion of the Rb vapor cell during installation.

The holder itself slides into the solenoid tube just far enough to position the Rb vapor cell in the middle thereof. An identical second standard holder slides into the solenoid tube from the opposite direction, fitting over the exposed end of the Rb vapor cell and stopping just before contacting the Rb vapor cell finger, as shown in Figure 9.2(b).

The "buffer gas" holder is identical to the standard holder, except for the depth of the cell-contacting hole; the depth is adjusted to position the shorter buffer gas cell in the middle of the solenoid tube and prevent the cell finger from contacting the holder.

Both sets of holders and the solenoid tube are constructed of delrin. Delrin is rigid enough to reliably hold the Rb vapor cell in the desired position without any motion, and

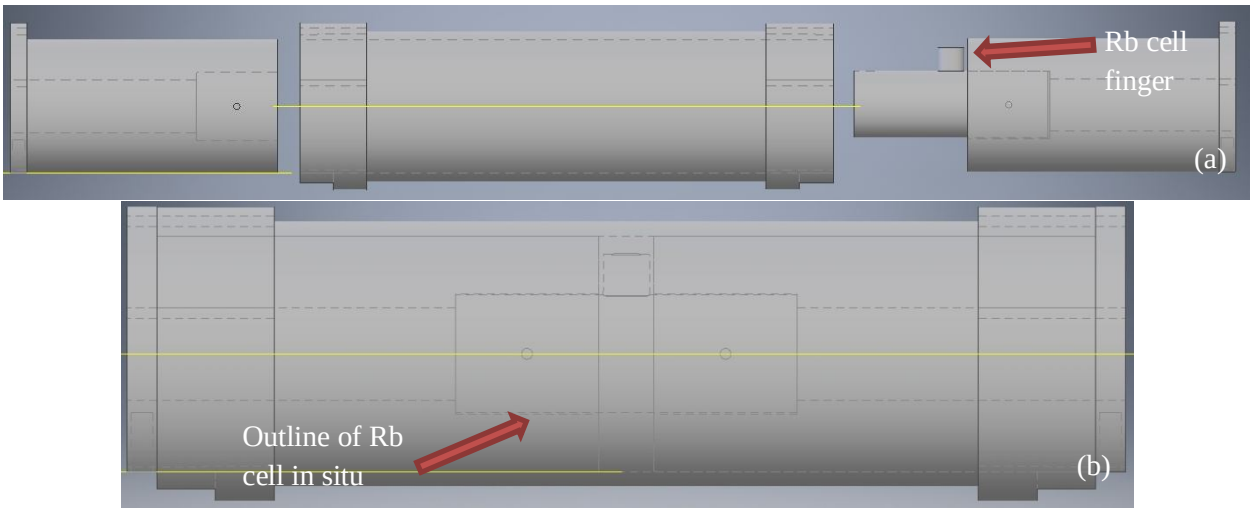

Figure 9.2 Schematic diagram of the Rb cell holders positioning a Rb cell. (a) From left to right, a standard Rb cell holder, the solenoid tube, and another standard Rb cell holder with a Rb vapor cell inserted. (b) The holders position the Rb vapor cell directly in the center of the solenoid tube.

additionally does not expand or deform much with heat. Although the heat resistance of delrin is not required for this thesis work, it is intended that these same holders and tube can be used in future experiments where the cell windows are heated.

9.2.2. Construction and Testing

The delrin holders and solenoid tube were fabricated by Jayson Alexander at the Miami University Instrumentation Lab.

To wrap the solenoid, we first measured out 3m of wire for connect the solenoid to the solenoid driver. We then anchored the wire to a bolt on one end of a standard Rb cell holder, and held the wire tight while rotating the solenoid tube. The wire used for wrapping the solenoid was not new, and had many kinks, twists, and coating defects that we needed to work around.

In order to straighten out the wire without cutting into the coating, we used a 2-1/4" PVC pipe. PVC is soft enough that the taught wire we intended to straighten would cut into our PVC pipe, rather than the pipe taking the coating off of the wire.

When we finished wrapping the first layer of the solenoid, we anchored the remaining wire using a bolt connected to the second solenoid holder, cleaned the wrapped wire with methanol, and ensured the wire was wound tightly and uniformly to the tube. Where the wrapping uniformity needed improvement, we used a wooden shim (the back end of a Q-tip) to

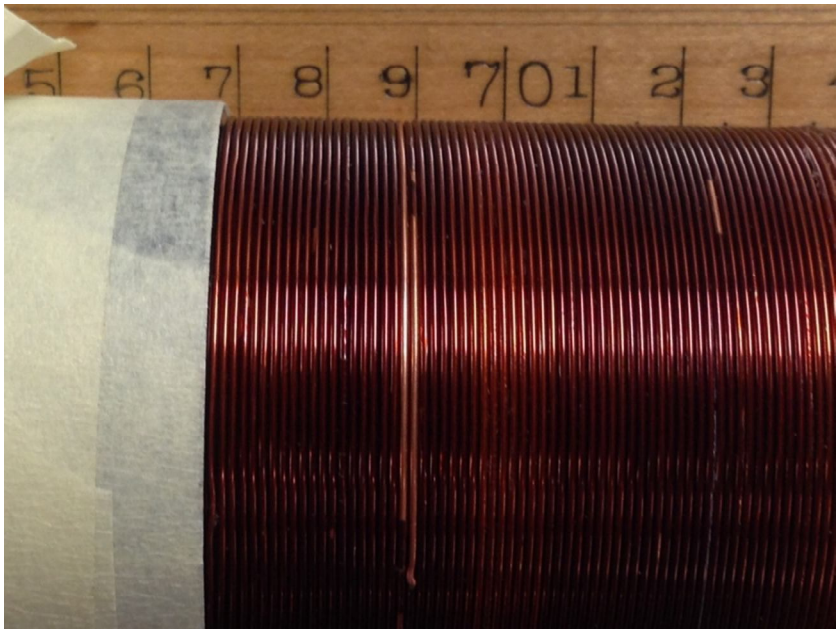

Figure 9.3 The wrapped solenoid tube. At the 69 cm mark, two consecutive turns of the solenoid are missing electrically insulating coating that would normally prevent a short.

push the wire closer together. Like the PVC tube, a wooden tightening implement was used to prevent damage to the coating on the wire.

We counted 170 turns for the first layer of wire, and observed one potential problem spot on the solenoid, where two uncoated sections of wire were adjacent to one another, as shown in Figure 9.3. To determine whether this section would introduce detrimental non-uniformity in the magnetic field, we decided to measure the magnetic field provided by just the first layer of the solenoid as shown in Figure 9.4(a). As shown in Figure 9.4(b), there is a small but notable non-uniformity in the magnetic field located about 4.5 cm from the center of the solenoid (at the 14 cm mark in the figure). As this non-uniformity occurs outside of the area containing the Rb vapor cell, we reasoned that it would not affect our experiment. From this measurement, we also determined that an applied current of 1 amp yields a magnetic field of 12.6 Gauss in the center of the solenoid. To attain magnetic fields comparable to those calculated for the previous solenoid, we needed another layer of 170 turns.

After wrapping a second layer of 170 turns and anchoring the wire in place, we again measured the magnetic field; the results are given in Figure 9.5 The peak magnetic field at the center of the region occupied by the standard Rb vapor cell is 25.36 Gauss, and at the edges the field drops to 23.75 Gauss, giving a variance over the cell region of 1.61 Gauss. As the buffer

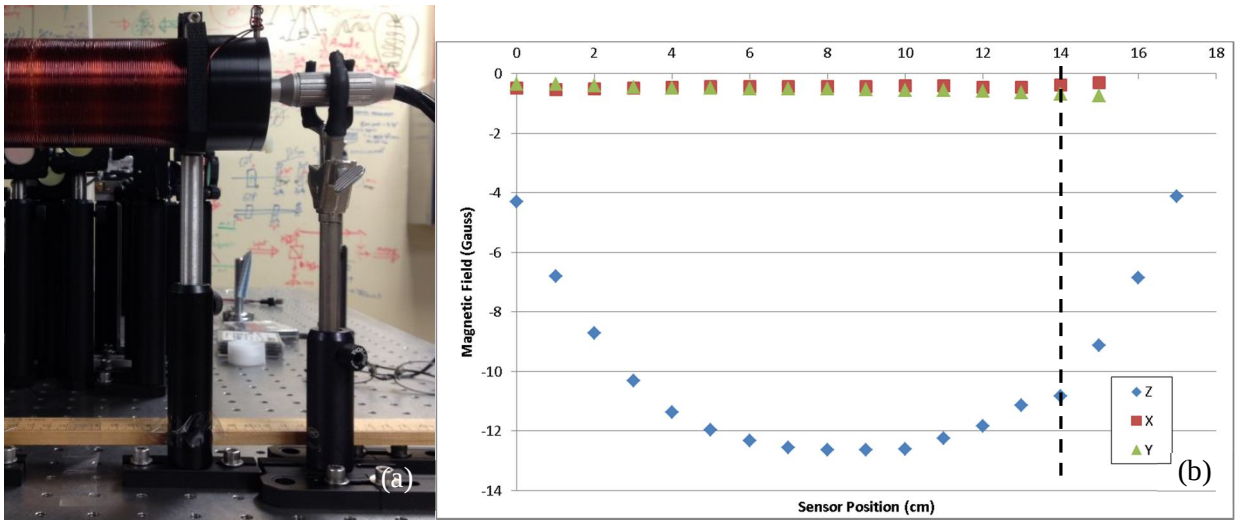

Figure 9.4 Magnetic field measurement apparatus and data. (a) Apparatus for measuring the magnetic field within the solenoid. A three-axis magnetic field probe is inserted into the solenoid, and the tip position is tracked using a meter stick. The mount for the probe is moved along rails, and the magnetic field is measured at each cm. (b) Measured magnetic field vs position for the first layer of the solenoid.

To preserve the position of the wires and reduce wear and tear on the wire coating, we decided to coat the solenoid with a spray-on rubber coating (Plasti Dip). We first covered the areas we did not want to coat with painters' tape, as shown in Figure 9.6(a). We then took the solenoid outside of the lab (to avoid jeopardizing other optics) and applied one heavy coat of Plasti Dip, before bringing it back in to dry for an hour. We applied four more coats of Plasti Dip in the same way, and finally left it to dry overnight. The finished product is shown in Figure 9.6(b).

The homogeneity of the magnetic field through the length of the vapor cell in Figure 9.5 represents a huge improvement over what the situation must have been in our previous experiment, which used the solenoid shown in Figure 8.2. The improvement is discussed further in Chapter 9.2.3.

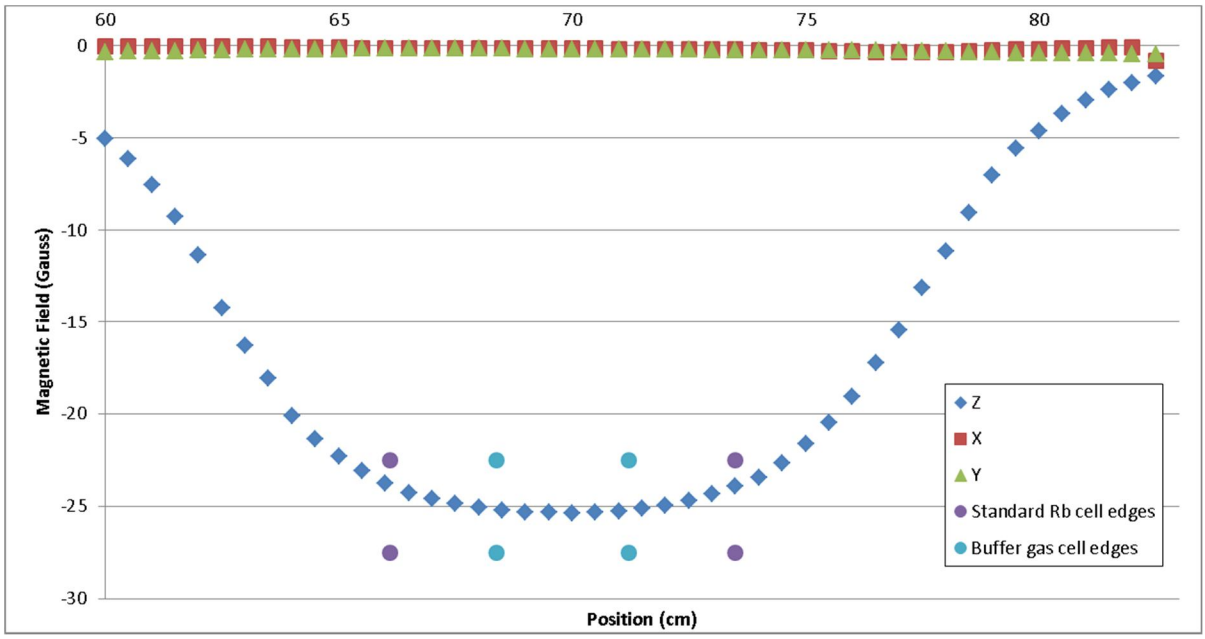

Figure 9.5 Measured magnetic field for the completed solenoid. The axial magnetic field peaks at -25.36 Gauss in the center of the cell. The edges of the standard and buffer gas Rb cells within this magnetic field are indicated. The edge of the solenoid tube is located at 80.6cm on the figure, and the edge of the solenoid is located at 77.5cm.

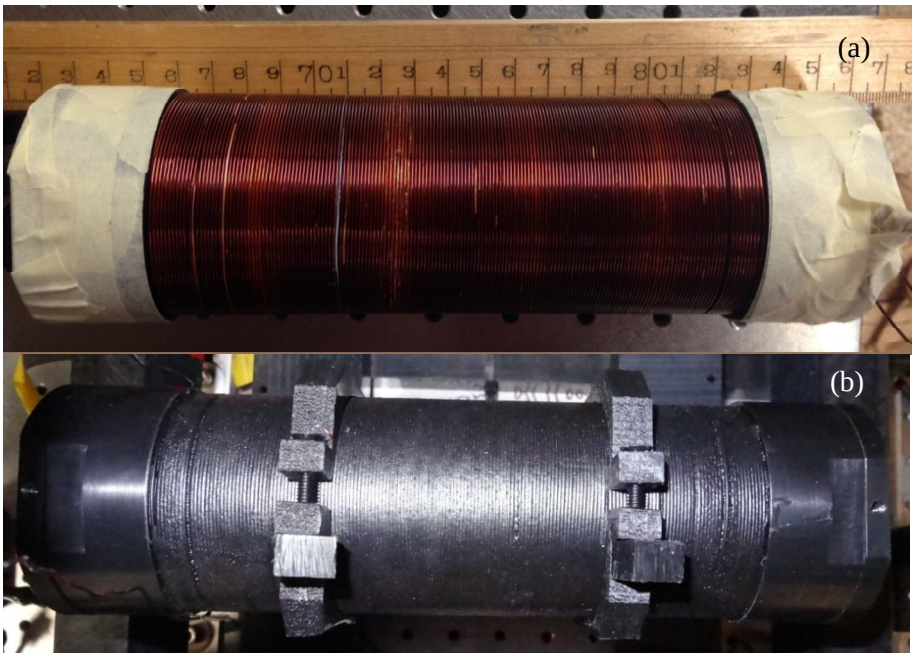

Figure 9.6 The wound solenoid (a) with painters' tape protecting the ends and inside of the assembly, and (b) finished assembly with Plasti Dip coating. Two C-clamps are shown holding the solenoid in position.

9.2.3. Magnetic Field Uniformity

The uniformity of the magnetic field within this new solenoid is significantly improved over that of the solenoid used in Chapter 7 and 8. This uniformity is brought about by two main improvements over the old solenoid: 1) the uniformity of the solenoid windings greatly improved, minimizing the generation of transverse magnetic fields by the solenoid itself, and 2) the new solenoid is significantly longer than the Rb vapor cell it was designed to fit, such that edge effects are much less of a concern.

The original solenoid consisted of magnetic wire wrapped directly around a standard Rb vapor cell. Due to the fragile nature of the Rb vapor cell especially in the vicinity of the cell finger, the windings of the solenoid could not be wrapped tightly around the cell. Additionally, the wire could not be wrapped uniformly in the vicinity of the finger, since the Rb vapor cell is not axially symmetric about this region. The loose windings and non-symmetric wrapping of this old solenoid allow for the generation of transverse magnetic fields, interfering with the experiment.

In the new solenoid, this has been remedied by specifically wrapping the windings around an axially symmetric and durable form. Accordingly, the windings could be wrapped

tightly and uniformly along the whole length of the solenoid, minimizing generation of off-axis magnetic fields.

For an ideal solenoid of finite length, the axial magnetic field is approximately uniform in the center of the solenoid lengthwise, decreases near the edge of the solenoid. These edge effects are clearly visible in the magnetic field measurements of the new solenoid shown in Figure 9.5, where the edge of the solenoid is located at 77.5 cm. In this case, the magnetic field at the edge of the solenoid is 13.11G, whereas the field in the center of the solenoid is 25.36G, giving a dropoff of 48.3%. For the region of the solenoid where a standard sized Rb vapor cell would be situated, however, the magnetic field only decreases to 23.75G, for a dropoff of 6.35%. For the region occupied by the buffer gas cell, this magnetic field only decreases to 25.06, for a dropoff of only 1.2%.

Since the old solenoid was wrapped directly around the glass walls of the Rb vapor cell, it was not possible for the solenoid to extend beyond the ends of the cell itself. In fact, the old solenoid is slightly shorter than the Rb vapor cell is wrapped around to accommodate the Teflon mounts by which the cell is held and by which the solenoid is held together. The dropoff between the middle and the edge of the Rb vapor cell inside of the old solenoid is conservatively estimated to be 50%.

9.2.4. Mounting

To hold the solenoid firmly in place, we designed and 3D printed two plastic C-clamps, visible in Figure 9.6(b). These C-clamps have one threaded hole for an 8-32” set screw, allowing them to be held in place by posts mounted to the table. The C-clamps are held shut using delrin screws and nuts so as to prevent any interaction with the magnetic field.

Unfortunately, the lab does not currently possess any non-magnetic posts or bases which could be used to connect the C-clamps to the table, so standard steel posts and holders were used for this purpose. These same steel posts and holders were used in the magnetic field measurements shown in Figure 9.4and Figure 9.6, but the effect thereof is not readily observed in the data.

9.3. Eliminating Electrical Noise

In order to eliminate the electrical noise seen in Figure 8.6-Figure 8.9, we increased the rate at which the magnetic field was scanned from 3Hz to 30Hz. At this frequency, the AC

electrical noise which permeated the results of the first experiment was reduced to a few discrete spikes in each of our recorded EIT/EIA features, as exemplified in Figure 9.7.

Since the 30Hz scan rate is slightly out of sync with the frequency of the noise spikes, the spikes slowly scroll across the screen. When taking data, we wait for these spikes to leave the vicinity of the EIT/EIA feature, pause the oscilloscope scan, and record a clean EIT/EIA feature.

9.4. Experimental Procedure

We were now ready to record the effect of relative angle between pump and probe beam on the EIT/EIA probe transmission spectra. The probe and pump powers were initially set to ≈ 100μW so that they are strong enough to be viewed when setting the relative pump/probe angle. The quarter wave plate after the Rb sample cell is temporarily removed, such that both beams are partially transmitted through the final polarizing beam splitter, and can be viewed in the far field. The separation between the pump and probe spots is measured at a distance of about 20m to obtain relative pump/probe angles. By adjusting the two mirrors in the probe path and viewing the separation between these pump and probe spots in the far field, the relative pump/probe angle can be set to a value between 0 and 1 milliradian.

After the desired relative angle is set, I_{probe} is set to ≈ 0.035 I_{sat}, and the quarter wave plate is replaced. The Zeeman splitting is scanned using the method described in Chapter 5.2.2, and

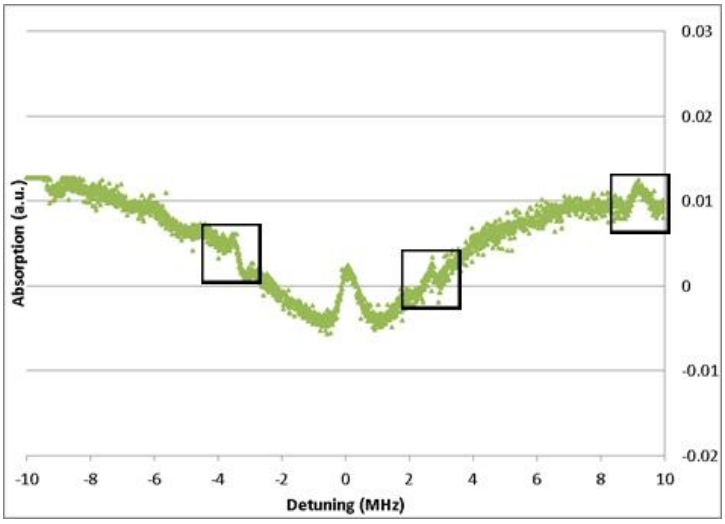

Figure 9.7 Example data for ^{85}Rb F_g=3 →F_e=2, 3, 4 EIA; three electrical noise spikes are in boxes. Over time, these spikes will drift from left to right in the feature because our chosen magnetic field scan frequency is out of sync with the electrical noise. By watching these drifts, we can assess whether spikes are interfering with the EIT/EIA feature, and determine when to record the oscilloscope trace.

the resulting EIT/EIA feature is recorded. This is repeated for both the ^{85}Rb F_g=2 →F_e=1, 2, 3 (EIT) and ^{85}Rb F_g=3 →F_e=2, 3, 4 (EIA) groups of transitions. This procedure is again repeated for each desired angle, and for two different pump powers, $I_{pump} \approx 8.7\ I_{sat}$ and $0.87\ I_{sat}$.

9.5. Preliminary Results

9.5.1. EIT vs. Pump/Probe Angle

The recorded EIT features for $I_{probe} = 0.035\ I_{sat}$ and $I_{pump} \approx 0.87\ I_{sat}$ pump power are shown in Figure 9.8 (a); those for $I_{pump} = 8.7\ I_{sat}$ are shown in Figure 9.8(b). The amplitude of the EIT features decreases with increasing angle, as shown in Figure 9.9(a), and their FWHM increases with angle, as shown in Figure 9.9(b).

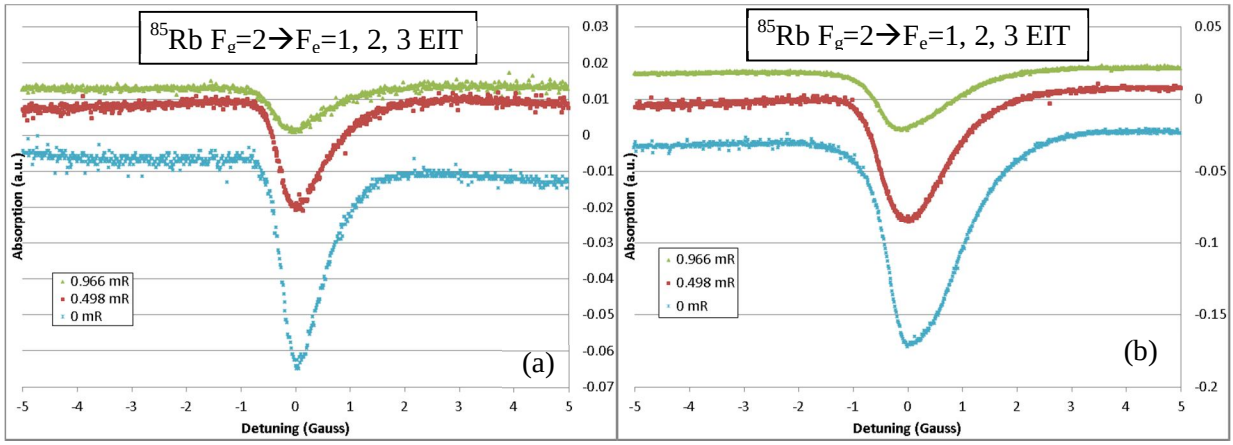

Figure 9.8 Probe absorption spectra showing EIT features for three relative pump/probe angles: 0.966, 0.498, and 0 milliradians. In the figures, $I_{probe} = 0.035\ I_{sat}$ and (a) $I_{pump} = 0.87\ I_{sat}$. (b) $I_{pump} = 8.7\ I_{sat}$. (a and b) No significant spurious pump- or probe-only features were observed for any of the tested angles.

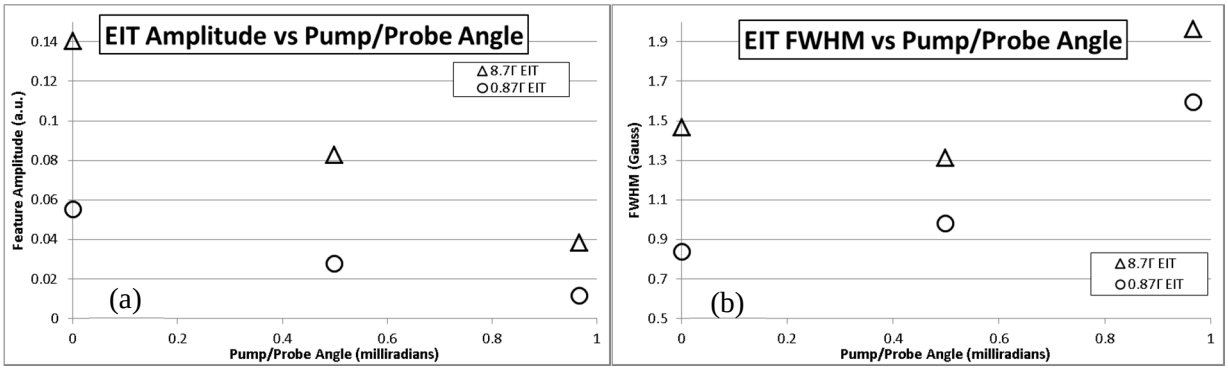

Figure 9.9 Lineshape data for the EIT features of Figure 9.8. (a) EIT feature amplitude vs. relative pump/probe angle. As the angle is increased, the amplitude of the feature decreases. (b) EIT feature FWHM vs. relative pump/probe angle. As the angle is increased, the FWHM of the feature increases.

9.5.2. EIA vs. Pump/Probe Angle

The recorded EIA features for I_{probe} = 0.035 I_{sat} and I_{pump} =0.87 I_{sat} are shown in Figure 9.10(a); those for I_{pump} =8.7 I_{sat} are shown in Figure 9.10(b). Just as for the EIT features, EIA features also decrease in amplitude with increasing angle as shown in Figure 9.11(a), and their FWHM also increases with angle, as shown in Figure 9.11(b).

9.6. Conclusions

As relative pump/probe angle increases, both EIT and EIA features decrease in amplitude and increase in FWHM. In order to determine the rate of increase or decrease, we decided to collect additional data for ^{5}Rb F_g=2 →F_e=1, 2, 3 (EIT).

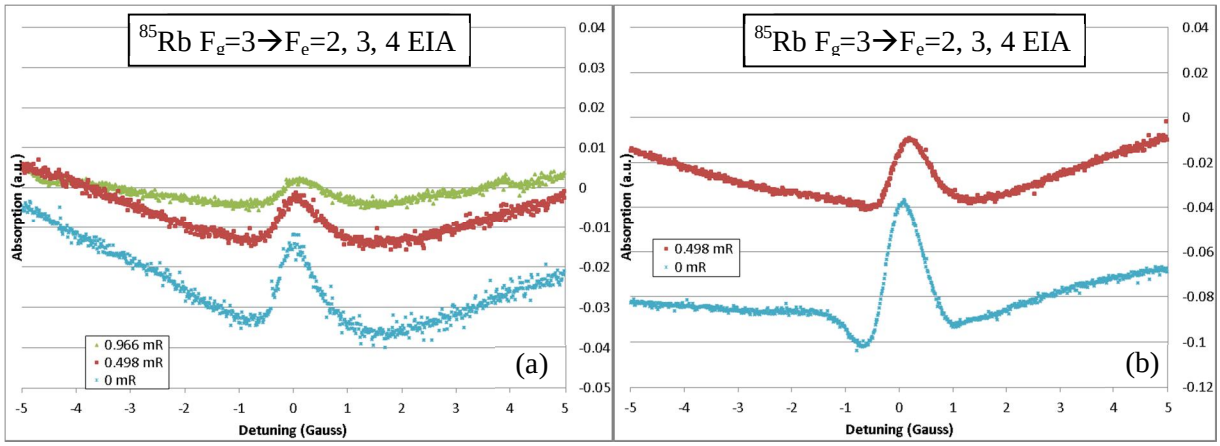

Figure 9.10 Probe absorption spectra showing EIA features for three relative pump/probe angles: 0.966, 0.498, and 0 milliradians. In the figures, I_{probe} = 0.035 I_{sat} and (a) I_{pump} = 0.87 I_{sat}. (b) I_{pump} = 8.7 I_{sat}. Corresponding data for 0.966 milliradians is missing at this power. (a and b) No spurious pump- or probe-only features were observed for any of the tested angles.

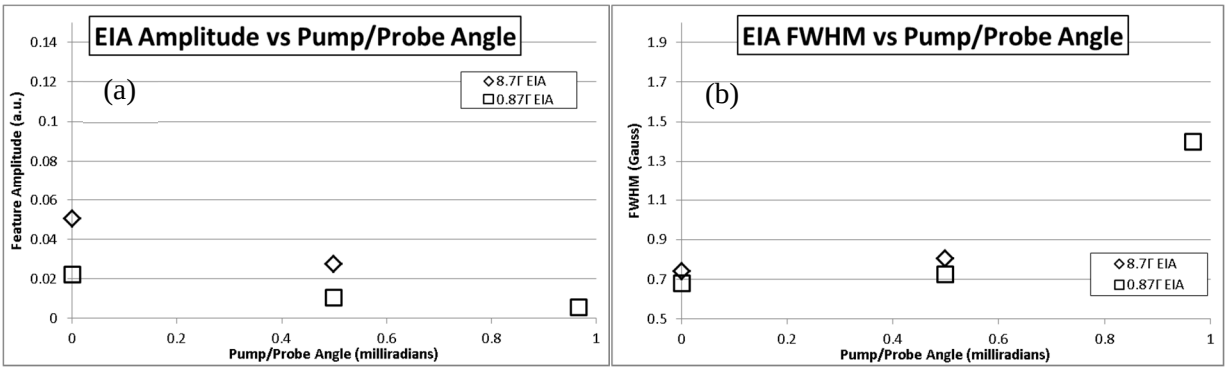

Figure 9.11 Lineshape data for the EIA features of Figure 9.10. (a) EIA feature amplitude vs. relative pump/probe angle. As the angle is increased, the amplitude of the feature decreases. (b) EIA feature FWHM vs. relative pump/probe angle. As the angle is increased, the FWHM of the feature increases.

9.7. Measurements of EIT Lineshape for Additional Relative Pump and Probe Angles

In order to further study the observed EIT amplitude and FWHM vs relative pump/probe angle, we decided to obtain data for additional angles on the ^{85}Rb $F_g=2 \rightarrow F_e=1, 2, 3$ transitions.

Before this experiment, we first optimized the pump beam alignment with the axial magnetic field. To do this, we blocked the probe beam and removed the quarter wave plate before the Rb cell. We observed the lineshape of the EIT feature obtained with just the linearly polarized pump beam while adjusting the pump propagation direction to minimize the FWHM of the feature. Once the feature FWHM was minimized, we replaced the quarter wave plate and unblocked the probe.

The pump and probe power were set to $I_{pump} \approx 4.4\ I_{sat}$ and $I_{probe} \approx 0.1\ I_{sat}$. The relative pump/probe angle was varied between 0 and 1 milliradian, and resultant EIT lineshapes were recorded (Figure 9.12). The observed EIT features appear symmetric for small angles, and become more asymmetric as the angle is increased. For large angles, the feature no longer resembles a Gaussian.

Due to the asymmetry of the observed features, we did not calculate FWHM. Instead, we determined the half width at half maximum (HWHM) for the left and right sides of each feature, and multiplied by two. Additionally, the EIT lineshapes for angles of 0.925, 0.789, and 0.539 milliradians appear too asymmetrical to assume that they follow a Gaussian trend; accordingly, HWHM data for these pump/probe angles was not considered. Plots of EIT feature amplitude

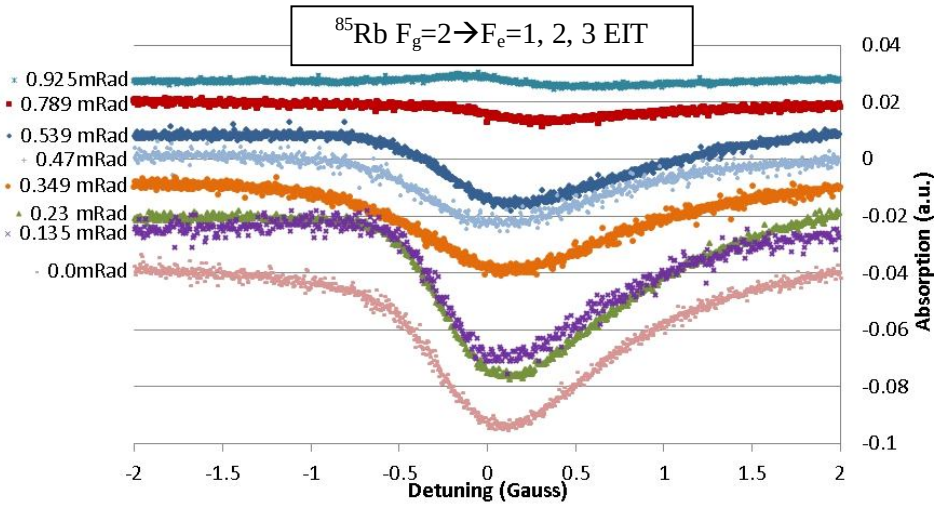

Figure 9.12 Recorded D2-line ^{85}Rb $F_g=2 \rightarrow F_e=1, 2, 3$ EIT features for angles between 0 and 1 milliradian. The pump and probe powers were $I_{pump} \approx 4.4\ I_{sat}$ and $I_{probe} \approx 0.1\ I_{sat}$.

and HWHM multiplied by 2 are shown in Figure 9.13 (a) and (b), respectively. A linear fit to the amplitude data can be made with an R^2 value of 0.8685.

The right-side HWHM of the EIT feature for $\theta = 0$, which was expected to have the smallest HWHM of the right-side data, is significantly broader than the other angles shown. The reason for this is not understood. Excluding this point, a linear fit to the average of the left & right HWHM data shown in Figure 9.13(b) can be made with an R^2 value of 0.6832 – the reason for this low value is the asymmetry in the absorption features. On the other hand, a quadratic fit to the HWHM data can be made with an R^2 value of 0.9102.

One possible source of the asymmetry is the scanning axial magnetic field, as discussed in Chapter 5.2.2. In order to reduce the asymmetry and obtain meaningful data for higher pump/probe angles, we consider that it is necessary to use a DC magnetic field and scan the probe frequency independently, as discussed in Chapter 5.2.1. For these reasons, we are working to modify our existing apparatus to observe Zeeman EIT/EIA in a DC magnetic field configuration, as discussed in the next chapter.

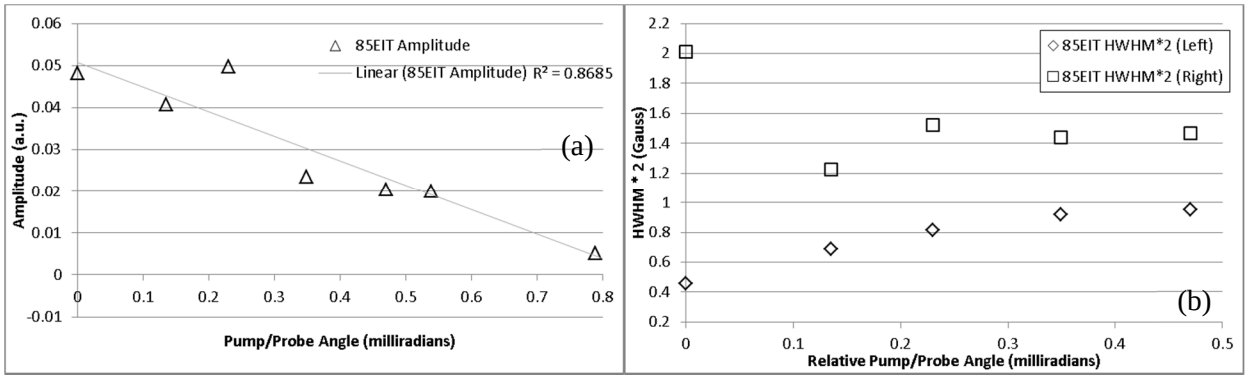

Figure 9.13 Lineshape data for the D2-line ^{85}Rb $F_g=2 \rightarrow F_e=1, 2, 3$ EIT features displayed in Figure 9.12. (a) EIT feature amplitude decreases as a function of pump/probe angle. (b) EIT feature (2)(HWHM) slightly increases as a function of pump/probe angle, and differences between left and right (2)(HWHM) show the asymmetry of the EIT features.

10. Progress toward Zeeman EIT/EIA using a DC magnetic field configuration

In this chapter, we report our progress on modifying our experimental apparatus to observe Zeeman EIT/EIA in the DC magnetic field configuration.

10.1. Objective

The drawbacks of using a scanning magnetic field configuration to observe Zeeman EIT/EIA were discussed in Chapter 5.2.2. Most important among these drawbacks is the inability to hold the pump detuning fixed while scanning the probe detuning. This inability makes understanding results very challenging as discussed in Chapter 8.4, introduces asymmetry as discussed in Chapter 9.7, and prevents us from benchmarking our experimental apparatus against peer-reviewed studies of EIT/EIA, such as those presented in [26, 40].

Accordingly, in this experiment, we switch to a DC magnetic field to control Zeeman splitting of the Rb hyperfine structure, and use acousto-optic modulators (AOMs) both to hold the pump frequency fixed and to scan the probe frequency around the pump.

10.2. Apparatus

The experimental setup is shown in Figure 10.1. This apparatus is the same as that used in Chapter 9.1, but now includes lenses and mirrors to focus the pump and probe beams into AOMs. The lenses have focal lengths of 15 and 20cm, to aid in exact positioning of each AOM at the

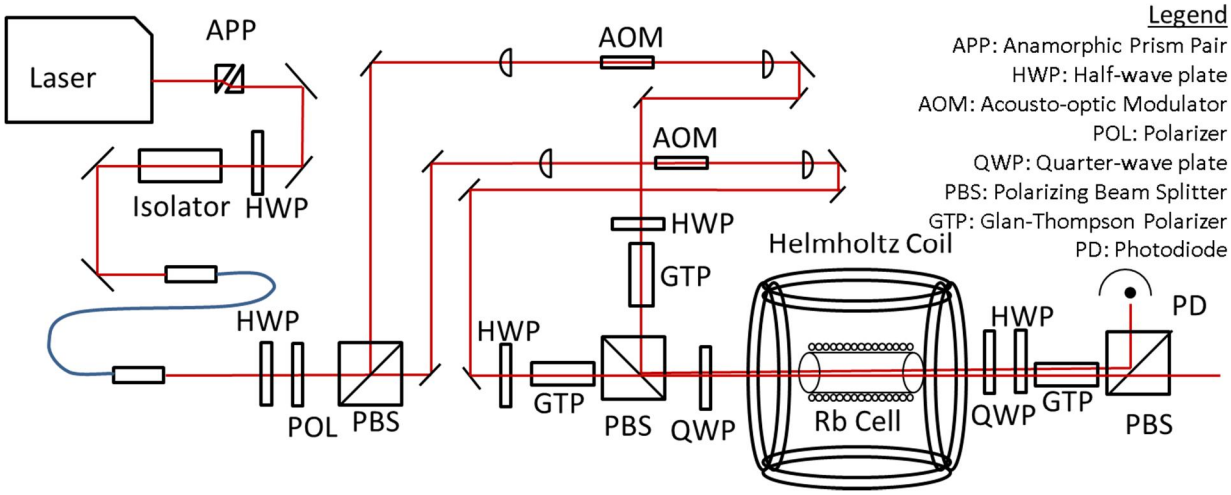

Figure 10.1 Experimental apparatus from Chapter 9.1, revised to send the pump and probe beams through single-pass AOMs. Lenses are used to focus the beams into and collimate the beams after the AOMs.

focal point. After the AOM, the +1 diffraction order is selected, imparting a frequency shift of the beam.

The amount of the frequency shift is controlled by an AOM driver. This driver applies an AC voltage to a piezoelectric transducer mounted to the AOM crystal. By adjusting the frequency at which the piezoelectric transducer vibrates, the amount of the frequency shift can be varied.

Due to space restrictions, it is not possible to put the 30cm- and 40cm-long AOM/lens assemblies directly in the existing setup of Chapter 9.1. Additional mirrors are used to direct the light to and from the setup. These additional mirrors also enable us to adjust the pump propagation direction, allowing us to minimize its angle with the axial magnetic field.

In normal operation, the laser slowly drifts away from resonance. To compensate for this in previous experiments, we manually adjusted the ECDL tuning by observing the saturated absorption spectra on an oscilloscope, centering the PZT-based tuning range on a desired frequency, and decreasing the amplitude of the tuning ramp to zero. Once the AOMs are installed, we will instead use a feedback loop to lock the laser to a desired frequency.

This is not only advantageous for frequency stability and measurement repeatability, but also provides a means by which to accurately measure the detuning of the pump and probe beams from resonance.

To date, we have installed one AOM and the associated mirrors and focusing optics in the probe beam path. As an initial goal, we are working to set the probe frequency to the ^{85}Rb F_g=2 $\rightarrow F_e$=1. To do this, we will lock the PZT frequency tuning on the left side of the ^{85}Rb F_g=2 $\rightarrow F_e$=2-3 crossover transition visible in the saturated absorption spectra. We will then use the AOM tuning range of 50-100MHz to red-tune by about 60MHz from this crossover transition, centering the beam on the ^{85}Rb F_g=2 $\rightarrow F_e$=1 hyperfine transition.

Out of the four groups of transitions available, we selected this transition because we have typically observed the largest D2-line EIT features using the ^{85}Rb F_g=2 $\rightarrow F_e$=1, 2, 3 group of transitions. ^{85}Rb F_g=2 $\rightarrow F_e$=1 in particular has comparably large transition strength as seen in Figure 5.6.

10.3. Experimental Procedure

The current through the solenoid will be held constant at 1Ampere, maintaining a DC magnetic field of 26 Gauss. The frequency of the pump is held in resonance with the m+1 transition via the use of one AOM, and a second AOM allows for the probe beam to be independently scanned around resonance with the m-1 transition.

The probe frequency is varied, and EIT/EIA features are observed as a function of probe detuning. As the probe detuning is now scanned independently of the pump detuning, we will finally be able to measure the linewidths of the observed EIT/EIA features in MHz, rather than in Gauss.

Once this experiment is completed, we will begin observing Zeeman EIT/EIA features at different relative pump/probe angles for comparison with those of Chapter 9. We will also perform the same measurements on a Rb vapor sample containing buffer gas, and compare our results to those obtained in Ref. [26]. The experiment for making these measurements is described briefly in the next section.

11. Future Experiment: Observation of Dicke Narrowing in Zeeman EIT/EIA as a function of relative pump/probe angle

11.1. Objective

This experiment has two main objectives. First, we intend to study the effect of pump/probe angle on EIT/EIA lineshapes in both a Rb vapor of natural abundance, and also a Rb vapor cell containing a buffer gas, using the D2-line transitions. To our knowledge, this has not been studied in the literature.

Second, we intend to directly compare the effect of pump/probe angle on EIT/EIA lineshapes in a Rb gas of natural abundance against the same effect in a sample containing buffer gas. Recall from Chapter 7.5 that the Dicke narrowed Doppler width is purported by [26] to have a quadratic dependence on pump/probe angle, and from Chapter 9.6 we observed an inverse dependence of EIT and EIA feature FWHM on relative pump/probe angle without the presence of a buffer gas. By this experiment, we wish to precisely determine the contribution of relative pump/probe angle to the effect of Dicke narrowing.

11.2. Experimental Procedure

The procedure will be performed using the apparatus of Figure 10.1.

Similar to the procedure of Chapter 9, the relative pump/probe angle will first be determined. This will be done by increasing the pump & probe intensities, removing the quarter wave plate after the sample to improve visibility of the beams, and measuring their displacement at a known distance in the far field. The quarter wave plate will be replaced, and the intensities will be adjusted to $I_{pump} \approx 9\ I_{sat}$ and $I_{probe} \approx 0.35\ I_{sat}$. A Zeeman EIT/EIA feature will be recorded for the standard Rb vapor cell. The cell will then be replaced with a buffer gas Rb vapor cell, and the measurement will be repeated for the identical pump/probe intensities and relative pump/probe angle as for the standard Rb vapor cell. The standard vapor cell will be replaced, and the procedure can be repeated for as many measurements as desired.

12. Conclusions and Future Outlook

We began by introducing the concepts of Electromagnetically Induced Transparency (EIT) and Absorption (EIA) in the traditional configuration, DC magnetic field Zeeman configuration, and scanning magnetic field Zeeman configurations. We theoretically modeled Zeeman EIT in a DC magnetic field configuration, and obtained a plot for a Fg=1 →Fe=0 atomic system. We discussed challenges to determination of EIT/EIA feature linewidths in a scanning magnetic field Zeeman configuration, and outlined our motivation to modify our experimental apparatus to employ a DC magnetic field Zeeman configuration. We also discussed the 85Rb and 87Rb atomic systems in which our experiments were performed, and explained the operation of our homebuilt external cavity diode laser.

Next, we used a single linearly polarized beam to observe Zeeman EIT in a scanning magnetic field configuration. When a quarter wave plate was installed to convert the beam to purely circular polarization, a large spurious EIT-like feature was observed. We determined that polarization impurity resulted in the observed spurious feature, and installed high extinction ratio Glan-Thompson polarizers to suppress and invert this spurious features.

In Chapter 7 we observed EIT/EIA using separate circularly polarized pump and probe beams. We determined that a relative angular separation between the pump and probe beams caused the light to become slightly elliptically polarized in the presence of a magnetic field, resulting in the same spurious features observed in Chapter 6. We also showed that relative pump/probe angles caused these two beams to undergo different Doppler shifts, effectively changing their detuning, and discussed Dicke narrowing as a method to suppress this Doppler shift mismatch.

In Chapter 7, we reconstructed and improved our experimental apparatus after relocating to a new building, adding a single-mode fiber and polarization filtering optics to enable observation of probe absorption spectra at very small relative pump/probe angles. We observed Zeeman EIT and EIA features in 85Rb and 87Rb at three different probe powers. Our experimental observations for 87Rb Fg=1 →Fe=0 EIT closely resemble our theoretical expectations from Chapter 5. We considered the effect of magnetic field nonuniformity on EIT/EIA lineshape, and noted observation of an ultranarrow EIA feature which was absent in observations made by another research group. We considered that we were able to observe this feature because of the small relative angle between our pump and probe beams.

In Chapter 9, we made improvements to our experimental apparatus to improve magnetic field uniformity and allow for switching between a standard Rb cell and a Rb cell including a buffer gas, paving the way for our future study of Dicke narrowing. We observed Zeeman EIT and EIA features in a scanning magnetic field configuration in 85Rb at a range of relative pump/probe angles from 0 and 1 milliradians. We affirmed that an increase in relative pump/probe angle both decreases amplitude and increases feature full width at half max. We noted an asymmetry in the observed EIT features, and considered that the asymmetry arose from the scanning magnetic field, further motivating us to modify our experiment to use a DC magnetic field configuration.

In Chapter 10, we began modifying our experimental apparatus to include acousto-optic modulators, such that we can observe Zeeman EIT/EIA in a DC magnetic field configuration. In this configuration, we plan to hold the pump frequency in resonance with the desired transition, and scan the probe frequency around resonance. We predicted that this will enable determination of observed EIT feature linewidths in MHz, greatly reduce asymmetry in the observed EIT/EIA spectral features, and greatly simplify our theoretical considerations of EIT and EIA.

Finally, we described a future experiment utilizing the improvements discussed in Chapter 10, wherein we will directly compare the effect of relative pump/probe angle on Zeeman EIT/EIA features observed in a Rb vapor with and without buffer gas.

13. Appendix

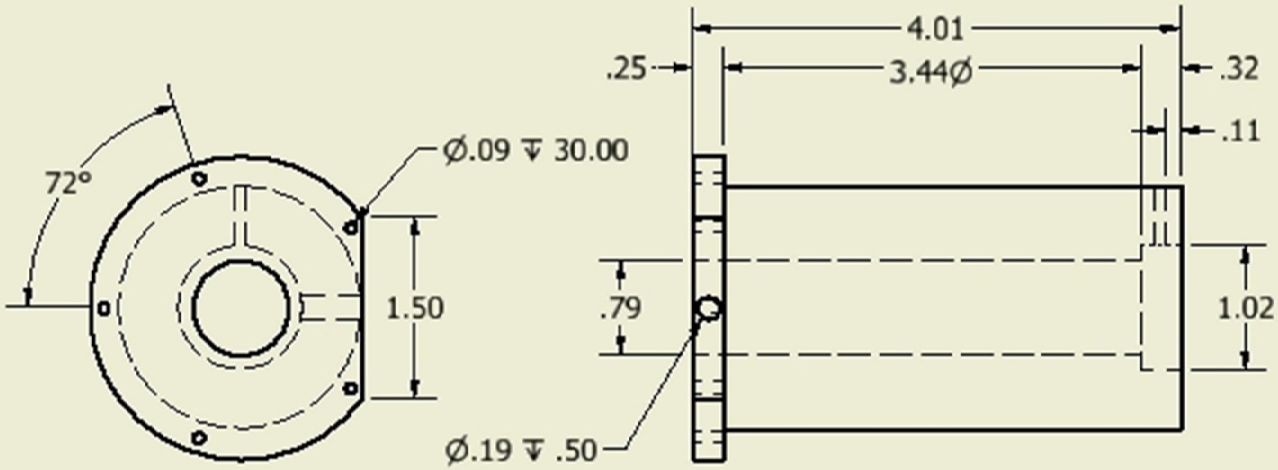

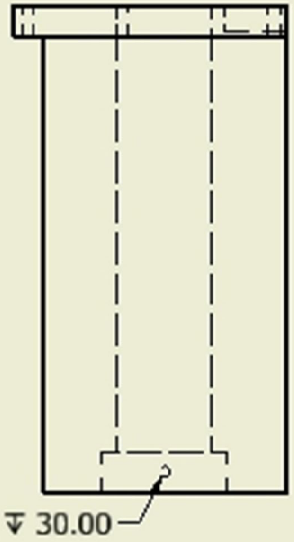

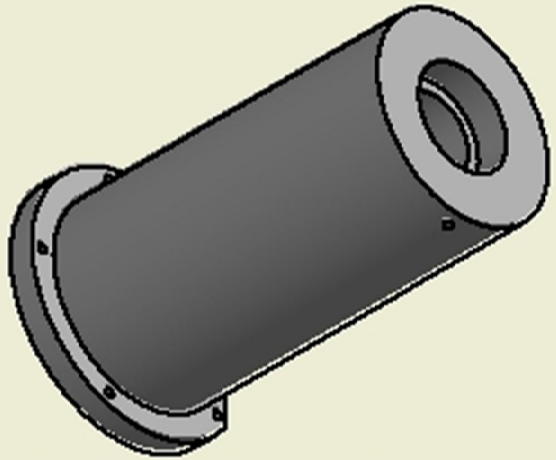

DRAWN Richard Jackson		Miami University	
CHECKED		TITLE Rb Buffer gas cell holder	
QA			
MFG			
APPROVED			
		SIZE A4	DWG NO Rb Buffer Cell Holder
		SCALE 2/3	SHEET 1 OF 1

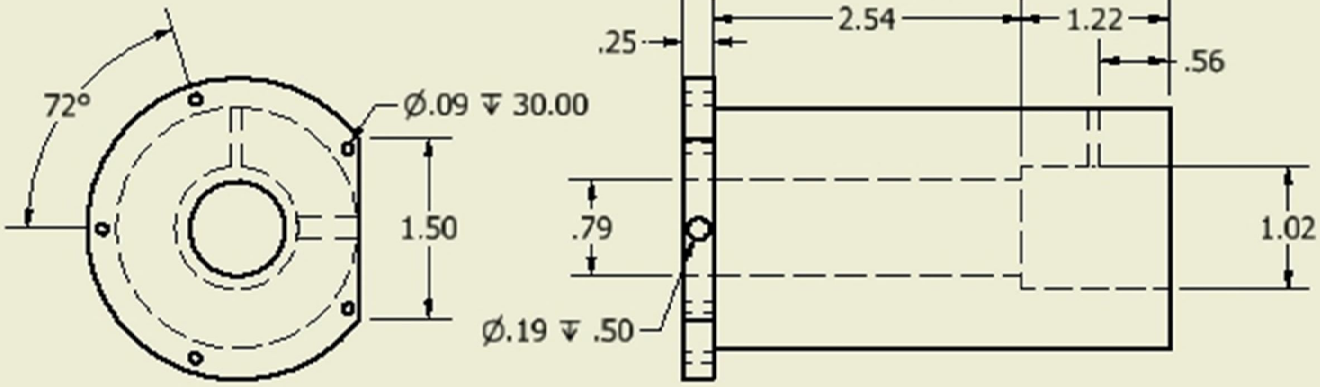

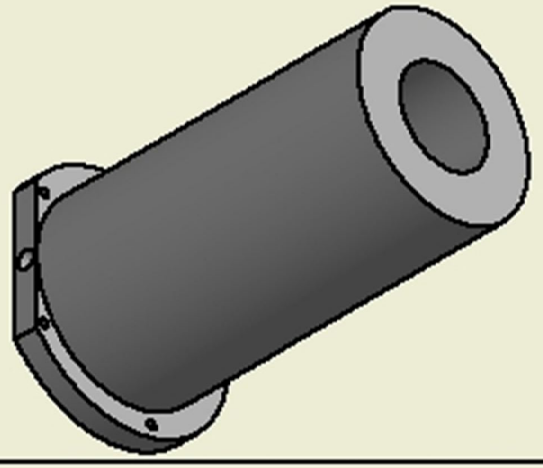

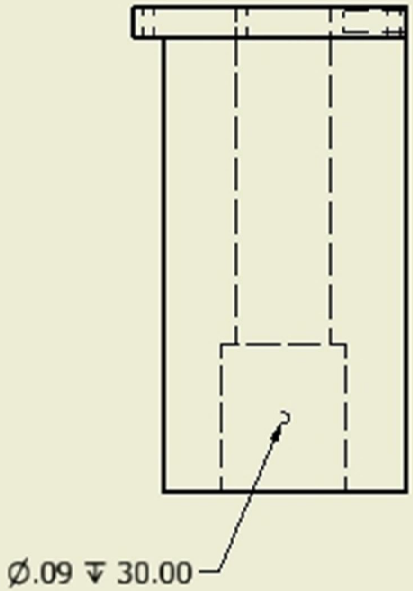

DRAWN Richard Jackson		Miami University
CHECKED		TITLE: Standard Rb Cell Holder
QA		
MFG		
APPROVED		
		SIZE A4 / DWG NO Standard Rb Cell Holder / REV
		SCALE 2/3 / SHEET 1 OF 1

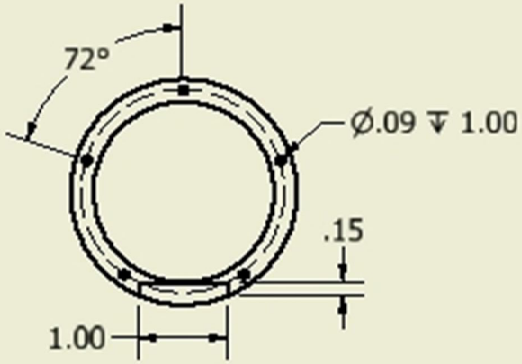

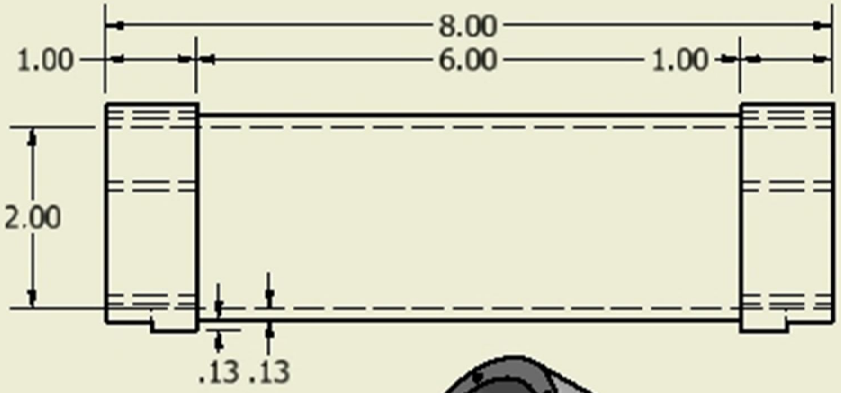

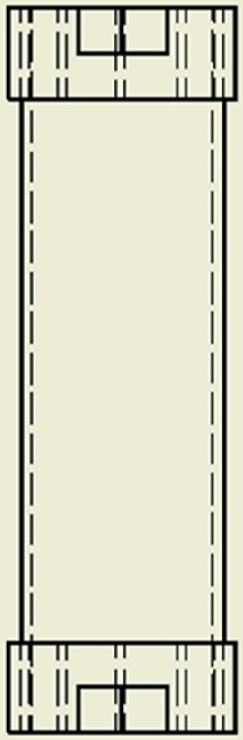

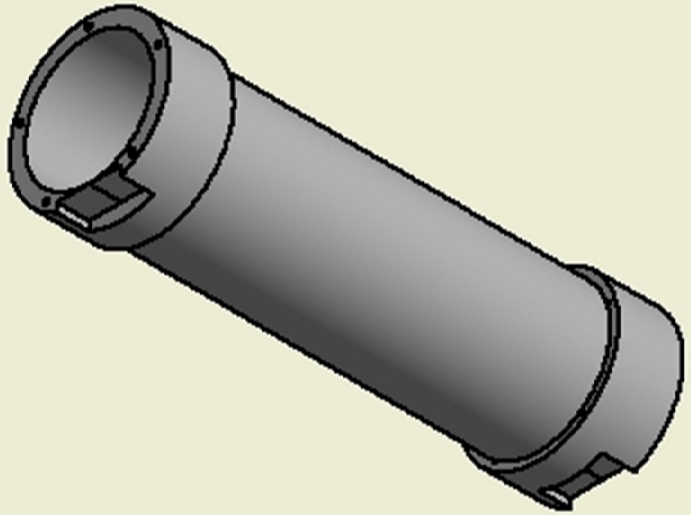

DRAWN Richard Jackson		Miami University	
CHECKED		TITLE	
QA		Solenoid Tube	
MFG			
APPROVED			
		SIZE A4	DWG NO Solenoid PVC tube
		SCALE 1/2	SHEET 1 OF 1

14. Bibliography

1. Dos Santos, F. B. M. & Macedo, A. M. S., Tuning Entanglement Patterns in Qubit Clusters. *J. Quant. Inf. Science* **3**, 85-92 (2013).

2. DiCarlo, L. *et al.*, Demonstration of two-qubit algorithms with a superconducting quantum processor. *Nature* **460** (08121) (2009).

3. Johnson, M. W. *et al.*, Quantum annealing with manufactured spins. *Nature* **473**, 194-198 (2011).

4. Martin-Lopez, E. *et al.*, Experimental realization of Shor's quantum factoring algorithm using qubit recycling. *Nature Photonics* **6**, 773-776 (2012).

5. Bao, X. *et al.*, Quantum teleportation between remote atomic-ensemble quantum memories. *PNAS* **109**, 20347-20351 (2012).

6. Zhou, Z., Lin, Q., Yang, M., Li, C. & Guo, G., Realization of Reliable Solis-State Quantum Memory for Photonic Polarization Qubit. *Phys. Rev. Lett.* **108** (190505) (2012).

7. Gundogan, M., Ledingham, P. M., Almasi, A., Cristiani, M. & Riedmatten, H., Quantum Storage of a Photonic Polarization Qubit in a Solid. *Phys. Rev. Lett.* **108** (190504) (2012).

8. Clausen, C., Bussieres, F., Afzelius, M. & Gisin, N., Quantum Storage of Heralded Polarization Qubits in Birefringent and Anisotropically Absorbing Materials. *Phys. Rev. Lett.* **108** (190503) (2012).

9. Saeedi, K. *et al.*, oom-Temperature Quantum Bit Storage Exceeding 39 Minutes Using Ionized Donors in Silicon-28. *Science* **342**, 830-833 (2013).

10. Benhelm, J., Kirchmair, G., Roos, C. F. & Blatt, R., Experimental quantum-information processing with 43Ca+ ions. *Phys. Rev. A.* **77**, 062306 (2008).

11. Morton, J. J. L. *et al.*, Solid-state quantum memory using the 31P nuclear spin. *Nature* **455**, 1085-1088 (2008).

12. Xu, Z. *et al.*, Long Lifetime and High-Fidelity Quantum Memory of Photonic Polarization Qubit by Lifting Zeeman Degeneracy. *Phys. Rev. Lett.* **111** (240503) (2013).

13. Dolde, F. *et al.*, High-fidelity spin entanglement using optimal control. *Nature Comm.* **5**, 3371 (2014).

14. Saito, S. *et al.*, Towards Realizing a Quantum Memory for a Superconducting Qubit. *Phys. Rev. Lett.* **111** (107008) (2013).

15. Heinze, G., Hubrich, C. & Halfmann, T., Stopped Light and Image Storage by Electromagnetically

Induced Transparency up to the Regime of One Minute. *Phys. Rev. Lett.* **111** (033601) (2013).

16. Riedmatten, H., Afzelius, M., Staudt, M. U., Simon, C. & Gisin, N., A solid-state light-matter interface at the single-photon level. *Nature* **456**, 773-777 (2008).

17. Eisaman, M. D. *et al.*, Optimizing the storage and retrieval efficiency of a solid-state quantum memory through tailored state preparation. *Proc. of SPIE* (67800K), 6780 (2007).

18. Liu, C., Dutton, Z., Behroozi, C. H. & Vestergaard, L., Observation of coherent optical information storage in an atomic medium using halted light pulses. *Nature* **409**, 490-493 (2001).

19. Kocharovskaya, O. A. & Khanin, Y. I., Population trapping and coherent bleaching of a three-level medium by a periodic train of ultrashort pulses. *Sov. Phys. JETP* **63** (5) (1986).

20. Schmidt, H. & Imamoglu, A., Giant Kerr nonlinearities obtained by electromagnetically induced transparency. *Opt. Lett.* **21** (1936) (1996).

21. Rebic, S., Tan, S. M., Parkins, A. S. & Walls, D. F., Large Kerr nonlinearity with a single atom. *J. Opt. B* **1**, 490-495 (1999).

22. Munro, W. J., Nemoto, K., Beausoleil, R. G. & Spiller, T. P., High-efficiency quantum-nondemolition single-photon-number-resolving detector. *Phys. Rev. A* **71** (033819) (2005).

23. Hetet, G., Pend, A., Johnsson, M. T., Hope, J. J. & Lam, P. K., Characterization of electromagnetically-induced-transparency-based continuous-variable quantum memories. *Phys. Rev. A* **77** (012323) (2008).

24. Vuclyasetu, P. K., Camacho, R. M. & Howell, J. C., Storage and Retrieval of Multimode Transverse Images in Hot Atomic Rubidium Vapor. *Phys. Rev. Lett.* **100** (123903) (2008).

25. Nicolas, A. *et al.*, A quantum memory for orbital angular momentum photonic qubits. *Nature Photonics* **8**, 234-238 (2014).

26. Shuker, M. *et al.*, Angular dependence of Dicke-narrowed electromagnetically induced transparency resonances. *Phys. Rev. A* **76** (023813) (2007).

27. Camacho, R. M., Broadbent, C. J., Ali-Khan, I. & Howell, J. C., All-Optical Delay of Images using Slow Light. *Phys. Rev. Lett.* **98** (043902) (2007).

28. Metcalf, H. J. & Straten, P. V. d., *Laser Cooling and Trapping* (Springer, New York, 2001).

29. Ashkin, A., Acceleration and Trapping of Particles by Radiation Pressure. *Phys. Rev. Lett.* **24**, 4 (1970).

30. Santa, I., Foggi, P., Righini, R. & Williams, J. H., Time-Resolved Optical Kerr Effect Measurements in Aqueous Ionic Solutions. *J. Phys. Chem.* **98**, 7692-7701 (1994).

31. Aitchison, J. S. *et al.*, Observation of spatial optical solitons in a nonlinear glass waveguide. *Opt. Lett.* **15**, 471-473 (1990).

32. Carvalho, P. R. S., Araujo, L. E. E. d. & Tabosa, J. W. R., Angular dependence of an electromagnetically induced transparency resonance in a Doppler-broadened atomic vapor. *Phys. Rev. A* **70** (063818) (2004).

33. Ye, C. Y. & Zibrov, A. S., Width of the electromagnetically induced transparency resonance in atomic vapor. *Phys. Rev. A* **62** (023806) (2002).

34. Dicke, R. H., The Effect of Collisions upon the Doppler Width of Spectral Lines. *Phys. Rev.* **89** (2) (1953).

35. Takamoto, M., Hong, F., Higashi, R. & Katori, H., An optical lattice clock. *Nature (London)* **435**, 321 (2005).

36. Boyd, M. M. *et al.*, Optical Atomic Coherence at the 1-Second Time Scale. *Science* **314** (1430) (2006).

37. Leibfried, D., Blatt, R., Monroe, C. & Wineland, D., Quantum dynamics of single trapped ions. *Rev. Mod. Phys.* **72**, 281 (2003).

38. Dancheva, Y., G. Alzetta, S. C., Taslakov, M. & Andreeva, C., Coherent effects on the Zeeman sublevels of hyperfine states in optical pumping of Rb by monomode diode laser. *Opt. Comm.* **178**, 103-110 (2000).

39. Rehman, H.-u., Adnan, M., Noh, H.-R. & Kim, J.-T., Spectral features of electromagnetically induced absorption in 85Rb atoms. *J. Phys. B: At. Mol. Opt. Phys.* **48**, 115502 (2015).

40. Firstenberg, O. *et al.*, Theory of Dicke narrowing in coherent population trapping. *Phys. Rev. A* **73** (013818) (2007).

41. Ram, N. & Pattabiraman, M., Sign reversal of Hanle electromagnetically Induced Absorption with Orthogonal Circularly Polarized Optical Fields. *J. Phys. B: At. Mol. Opt. Phys.* **43**, 245503 (2010).

42. Ram, N., Pattabiraman, M. & Vijayan, C., Effect of ellipticity on Hanle electromagnetically induced absorption and transparency resonances with longitudinal and transverse magnetic fields. *Phys. Rev. A* **82**, 033417 (2010).

43. Ram, N., Anupriya, J., Pattabiraman, M. & Vijayan, C., Role of transfer of coherence in the enhanced absorption Hanle Effect with Two Optical Fields. *J. Phys. B: At. Mol. Opt. Phys.* **42**, 175504 (2009).

44. Ram, N., PhD Thesis, 2011 (Indian Institute of Technology Madras).

45. Zhou, L., Characterizing Hyperfine Structures in 87Rb and 85Rb with Doppler-Free Spectroscopy. *MIT database* (2013).

46. Steck, D. A., Rubidium D Line Data, Available at http://steck.us/alkalidata/rubidium85numbers.pdf (2008).

47. Steck, D. A., Rubidium 87 D Line Data, Available at http://steck.us/alkalidata/rubidium87numbers.pdf (2001).

48. Barkeloo, J., Masters Thesis, 2012 (Miami University).

49. Day, A., Masters Thesis, 2013 (Miami University).

50. Worth, B. I., Masters Thesis, 2013 (Miami University).

51. MacAdam, K. B., Steinbach, A. & Wieman, C., A Narrow-band tunable diode laser system with grating feedback, and a saturated absorption spectrometer for Cs and Rb. *A. J. Phys.* **60** (12), 1098 (1992).